

Evaluating the impact of new observational constraints on P-S/IVOC emissions, multi-generation oxidation, and chamber wall losses on SOA modeling for Los Angeles, CA

Prettiny K. Ma,¹ Yunliang Zhao,² Allen L. Robinson,² David R. Worton,^{3,a} Allen H. Goldstein,^{3,4} Amber M. Ortega,^{5,b} Jose L. Jimenez,⁵ Peter Zotter,^{6,c} André S. H. Prévôt,⁶ Sönke Szidat,⁷ and Patrick L. Hayes¹

¹Department of Chemistry, Université de Montréal, Montréal, QC, Canada

²Center for Atmospheric Particle Studies, Carnegie Mellon University, Pittsburgh, PA, USA

³Department of Environmental Science, Policy and Management, University of California, Berkeley, CA, USA

⁴Department of Civil and Environmental Engineering, University of California, Berkeley, CA, USA

⁵Cooperative Institute for Research in the Environmental Sciences and Dept. of Chemistry and Biochemistry, University of Colorado, Boulder, CO, USA

⁶Laboratory of Atmospheric Chemistry, Paul Scherrer Institute, Villigen, Switzerland

⁷Department of Chemistry and Biochemistry & Oeschger Centre for Climate Change, University of Bern, Bern, Switzerland

^anow at: National Physical Laboratory, Hampton Rd, Teddington, Middlesex, UK

^bnow at: Air Pollution Control Division, Colorado Department of Public Health and Environment, Denver, CO, USA

^cnow at: Lucerne University of Applied Sciences and Arts, School of Engineering and Architecture, Bioenergy Research, Technikumstrasse 21, CH-6048 Horw, Switzerland

Correspondence to: Patrick L. Hayes (patrick.hayes@umontreal.ca)

28 **ABSTRACT**

29 Secondary Organic Aerosols (SOA) are important contributors to fine PM mass in
30 polluted regions, and their modeling remains poorly constrained. A box model is
31 developed that uses recently published literature parameterizations and data sets to better
32 constrain and evaluate the formation pathways and precursors of urban SOA during the
33 CalNex 2010 campaign in Los Angeles. When using the measurements of IVOCs
34 reported in Zhao et al. (2014) and of SVOCs reported in Worton et al. (2014) the model
35 is biased high at longer photochemical ages whereas at shorter photochemical ages it is
36 biased low, if the yields for VOC oxidation are not updated. The parameterizations using
37 an updated version of the yields, which takes into account the effect of gas phase wall-
38 losses in environmental chambers, show model/measurement agreement at longer
39 photochemical ages, even though some low bias at short photochemical ages still
40 remains. Furthermore, the fossil/non-fossil carbon split of urban SOA simulated by the
41 model is consistent with measurements at the Pasadena ground site.

42 Multi-generation oxidation mechanisms are often employed in SOA models to
43 increase the SOA yields derived from environmental chamber experiments in order to
44 obtain better model/measurement agreement. However, there are many uncertainties
45 associated with these “aging” mechanisms. Thus, SOA formation in the model is
46 compared against data from an oxidation flow reactor (OFR) in order to constrain SOA
47 formation at longer photochemical ages than observed in urban air. The model predicts
48 similar SOA mass at short to moderate photochemical ages when the “aging”
49 mechanisms or the updated version of the yields for VOC oxidation are implemented.
50 The latter case though has SOA formation rates that are more consistent with
51 observations from the OFR. Aging mechanisms may still play an important role in SOA
52 chemistry, but the additional mass formed by functionalization reactions during aging
53 would need to be offset by gas-phase fragmentation of SVOCs.

54 All the model cases evaluated in this work have a large majority of the urban SOA
55 (70 – 83 %) at Pasadena coming from the oxidation of P-SVOCs and P-IVOCs. The
56 importance of these two types of precursors is further supported by analyzing the
57 percentage of SOA formed at long photochemical ages (1.5 days) as a function of the
58 precursor rate constant. The P-SVOCs and P-IVOCs have rate constants that are similar
59 to highly reactive VOCs that have been previously found to strongly correlate with SOA
60 formation potential measured by the OFR.

61 Finally, the volatility distribution of the total organic mass (gas and particle
62 phase) in the model is compared against measurements. The total SVOC mass simulated
63 is similar to the measurements, but there are important differences in the measured and
64 modeled volatility distributions. A likely reason for the difference is the lack of particle-
65 phase reactions in the model that can oligomerize and/or continue to oxidize organic
66 compounds even after they partition to the particle phase.

1. INTRODUCTION

Atmospheric aerosols are important climate forcing agents (Christensen et al., 2013), negatively impact human health (Dockery and Pope, 1994) and reduce visibility by scattering and absorbing light (Watson, 2002). However, predicting quantitatively the composition and concentrations of aerosols is challenging, in part because of their complex composition and the variety of emission sources and chemical pathways that contribute to aerosol loadings in the atmosphere (Heald et al., 2011; Spracklen et al., 2011). Atmospheric aerosols are composed of black carbon, inorganic, and organic matter, and the latter is a mixture of hundreds to thousands of compounds (Gentner et al., 2012).

Due to this complexity, organic aerosol is often categorized into two groups. Primary organic aerosol (POA) is directly emitted into the atmosphere from sources such as motor vehicles, food cooking, and biomass burning (Hallquist et al., 2009). On the other hand, secondary organic aerosol (SOA) is the product of diverse chemical reactions occurring in the atmosphere that transform more-volatile precursors such as volatile organic compounds (VOCs) into lower volatility products that are either incorporated into existing particles or form new particles. Many previous studies have shown that SOA is an important fraction of OA globally often representing more than half the total OA concentration (Zhang et al., 2007; Jimenez et al., 2009).

In SOA parameterizations for use in regional and global models, a semi-empirical approach is used in which VOCs, often the only SOA precursors considered, react with OH radicals and other oxidants to form secondary products with lower volatility at a given mass yield. These secondary semi-volatile organic compounds (SVOCs) can partition to the particle phase to form SOA (Pankow, 1994; Odum et al., 1996; Donahue et al., 2006). The parameters used in the models for the VOCs, such as the yields and product volatilities, are often determined from published chambers studies (e.g. Kroll et al., 2006; Chan et al., 2009; Hallquist et al., 2009; Presto et al., 2010). Over the past decade a number of studies have shown that traditional models that consider only the oxidation of VOCs alone predict SOA concentrations much lower than those observed in polluted urban regions (Volkamer et al., 2006; Dzepina et al., 2009; Hodzic and Jimenez, 2011; Hayes et al., 2015). As a result, several updates have been proposed in the literature to improve SOA models including new pathways for SOA formation, new SOA precursors, and increased yields for known precursors (e.g. Ng et al., 2007; Robinson et al., 2007; Ervens and Volkamer, 2010).

The volatility basis-set (VBS) approach (Donahue et al., 2006) has been used in most recent parameterizations of SOA yields. In this approach, the organic mass is distributed in logarithmically spaced volatility bins, and the SOA forming reactions then redistribute the mass from precursors such as anthropogenic and biogenic VOCs, into

bins with generally lower volatility (except for fragmentation reactions) leading to increased OA concentrations (Robinson et al., 2007; Tsimpidi et al., 2010). While the VBS provides a valuable conceptual framework for SOA modeling, substantial uncertainties remain in the correct parameters for different precursors and conditions.

In this paper we focus on investigating three interrelated questions that are responsible for important uncertainties in urban SOA modeling. The first is how to best incorporate SOA from primary semi- and intermediate volatility compounds (P-S/IVOCs), two recently-proposed types of SOA precursors. While there is now ample evidence that P-S/IVOCs are important contributors to SOA (Robinson et al., 2007; Zhao et al., 2014; Dunmore et al., 2015; Ots et al., 2016), the emissions of these precursors as well as the parameters that govern their oxidation and SOA formation are not well constrained. Also, it is well known that models of SOA that incorporate P-S/IVOCs often do not agree with measurements across a range of photochemical ages, although the modeled SOA mass varies substantially with the parameterization used (Dzepina et al., 2009; Hayes et al., 2015; Fountoukis et al., 2016; Woody et al., 2016). The second question is whether losses of semi-volatile gases to the walls of environmental chambers (Matsunaga and Ziemann, 2010; Krechmer et al., 2016) have resulted in low biases for the yields of some or all precursors, especially VOCs, as has been recently reported (Zhang et al., 2014). The third question is the appropriateness of including “aging” mechanisms in the VBS parameterization of SOA from VOCs, in which the initial oxidation reaction is followed by subsequent oxidation reactions of the first and later generation products, with each reaction resulting in a reduction of the organic volatility by, for example, an order of magnitude. These “aging” mechanisms increase VOC yields to levels much higher than those observed in chamber studies since it was perceived that the yields may be too low in chambers compared to the real atmosphere. The “aging” mechanisms were added to chamber yields that were obtained without using aging as part of the fits of the chamber data. In some model applications they improve model agreement with field measurements (Ahmadov et al., 2012), while at long photochemical ages they lead to model SOA formation that is substantially larger than observed (e.g. Dzepina et al., 2011; Hayes et al., 2015). While the inclusion of some of these new SOA precursors, updated yields, and aging can provide in some cases better agreement with measurements, the relative amount of SOA formed from VOCs (V-SOA), P-IVOCs (I-SOA), and P-SVOCs (S-SOA) is highly uncertain, and changes strongly depending on which of the above updates are implemented in a specific model. In addition, the fact that different subsets and variants of these updates can allow specific models to match SOA measurements raises important questions regarding whether or not the model mechanisms are representative of actual SOA forming processes in the atmosphere.

The notation used when discussing SOA precursors in this paper is similar to Hayes et al. (2015). We differentiate VOCs, IVOCs and SVOCs by their effective saturation concentration (c^*). Therefore, SVOCs and IVOCs have volatilities ranging from $c^* = 10^{-2}$ to 10^2 and 10^3 to $10^6 \mu\text{g m}^{-3}$ respectively, while VOCs are in the bins of $c^* \geq 10^7 \mu\text{g m}^{-3}$.

Recently, we evaluated three parameterizations for the formation of S-SOA and I-SOA using a constrained 0-D box model that represents the South Coast Air Basin during the California Research at the Nexus of Air Quality and Climate Change (CalNex) campaign (Hayes et al., 2015). Box models are often used to compare with ambient measurements, and have been shown to be of similar usefulness or even superior to 3-D models if the emissions and atmospheric transport affecting a given case study are well constrained, and if the use of ratios to tracers can be used to approximately account for dispersion (e.g. Volkamer et al., 2006; Dzepina et al., 2009; Hayes et al., 2015; Yuan et al., 2015). A box model allows the evaluation of multiple model parameterizations either previously proposed in the literature or developed from recent field and laboratory data sets, as well as the performance of sensitivity studies, all of which would be difficult to carry-out in more computationally demanding gridded 3-D models. There are six model cases presented in this paper that are described in further detail below. Given the number of model cases (including three additional model cases from Hayes et al. (2015)), it would be very computationally expensive to use a 3-D model to evaluate all the cases.

Moreover, there are important limitations to traditional comparisons of 3-D models' predicted concentrations against measurements, as for example discussed for the Pasadena ground site in Woody et al. (2016). In that study, the SOA predicted by the Community Multiscale Air Quality (CMAQ) model with a VBS treatment of OA is a factor of 5.4 lower than the measurements during the midday peak in SOA concentrations. This underestimation was attributed to several different factors. First, the model photochemical age for the site was too low by a factor of 1.5. In the box model presented in this current work, that problem is eliminated as the photochemical aging of the urban emissions in the model is instead determined from the measured ratio of 1,2,4-trimethylbenzene to benzene as described previously (Parrish et al., 2007; Hayes et al., 2013). Second, it is difficult to distinguish errors due to model dispersion from those due to emission inventories and photochemical age. Woody et al. (2016) conclude that excessive dispersion or low emissions account for an error of about a factor of 2. Those errors are also eliminated by the use of emission ratios in this work. After those errors are accounted for, by analyzing the 3-D model output using similar techniques as in our box model, the real under-prediction of SOA formation efficiency by a factor of 1.8 emerged, compared to the initial value of 5.4 from the concentration comparisons. These errors (of approximately 300%) in the interpretation of 3-D model comparisons, which are ignored

181 in most 3-D model studies, are far larger than the uncertainties due to emission ratios or
182 dispersion in our box model (about 10 - 20%), as demonstrated in section 2.4.

183 In addition, there are uncertainties in the P-S/IVOC emissions inventories used in
184 3-D models and in the methods used to estimate P-S/IVOC emissions from the traditional
185 POA inventories. In our box model, as described in further detail below, we incorporated
186 recently published field measurements of P-S/IVOCs to better constrain the concentration
187 of these species. Thus, while 3-D models are essential for simulating spatially and
188 temporally complex environments under the influence of many sources, in cases where
189 transport is relatively simple and there is a well-defined urban plume such in Pasadena
190 during the CalNex campaign, the box model is a valuable complementary or even
191 superior approach that is less susceptible to the convoluted uncertainties in 3-D models
192 discussed above. Another reason to use a box model is that it allows a direct comparison
193 against OFR measurements taken in the field (Ortega et al., 2016). The OFR provided
194 (every 20 minutes at the Pasadena ground site) a measure of SOA formation potential for
195 a photochemical age of up to two weeks. To the best of our knowledge, 3-D models have
196 not yet been adapted for comparison against OFR data. Finally, box models are more
197 widely usable by experimental groups (such as ours) due to reduced complexity, while
198 3-D models are almost exclusively used by modeling-only groups, who tend to be more
199 distant from the availability, use, and interpretation of experimental constraints. Thus the
200 use of a range of models by a range of different groups is highly beneficial to scientific
201 progress.

202 The results obtained in our previous work (Hayes et al., 2015) using a box model
203 indicated that different combinations of parameterizations could reproduce the total SOA
204 equally well even though the amounts of V-SOA, I-SOA, and S-SOA were very different.
205 In addition, the model over-predicted SOA formed at longer photochemical ages (\approx 3
206 days) when compared to observations downwind of multiple urban sites. This
207 discrepancy suggests that the ratio of P-S/IVOCs-to-POA may have been too high in the
208 parameterizations evaluated. Also, as mentioned previously and discussed in Hayes et al.
209 (2015), the implementation of aging for VOC products remains uncertain.

210 The goal of this study is to use several recently published results to better evaluate
211 and constrain the box model introduced in our previous work, and thus facilitate the
212 identification of parameterizations that can be eventually incorporated into 3-D air
213 quality models to accurately predict SOA for the right reasons. It is important to note that
214 parameterizations used in the box model are based on several published measurements
215 taken from laboratory experiments and field studies that provide more realistic
216 constraints than in previous versions and that were not available to be implemented in
217 Hayes et al. (2015). In particular, our work here improves the box model by incorporating
218 recently published measurements of P-IVOCs and P-SVOCs that allow better
219 constraining of the concentration, reactivity, yields, and volatility of these precursors

(Worton et al., 2014; Zhao et al., 2014). In addition, given that experiments in environmental chambers may underestimate SOA yields for the VOCs due to losses of semi-volatile gases to the chamber walls (Zhang et al., 2014), the SOA yields from VOCs have been re-estimated using a very recent parameterization of these wall-losses (Krechmer et al., 2016). The wall-loss corrected yields obtained are then used in the model in a sensitivity study to evaluate the corresponding change in the modeled SOA concentrations. The model is modified based on these literature constraints. No model tuning is performed with the goal of improving the agreement with the observations. The results obtained from the new box model are compared against ambient ground site and airborne measurements, and also against recently-published oxidation flow reactor (OFR) measurements (Ortega et al., 2016). This combination of data sets allows the model to be evaluated for photochemical ages ranging up to 3 equivalent days (at 1.5×10^6 molec OH cm^{-3}) providing a means to evaluate the aging mechanisms of the VOCs in the VBS.

2. EXPERIMENTAL SECTION

2.1 Measurement and sampling site

The box model is constructed in order to represent the South Coast Air Basin during CalNex in spring/summer 2010. The measurements of aerosols used in this study were conducted in Pasadena, California (34.1406° N 118.1224° W), located to the northeast of downtown Los Angeles (Hayes et al., 2015). An overview of CalNex has been published previously (Ryerson et al., 2013). The location and the meteorology of the ground site at Pasadena are described in further detail in Hayes et al. (2013). Pasadena is a receptor site for pollution due to winds that transport emissions from the Ports of Los Angeles and Long Beach and downtown Los Angeles. Airborne measurements of aerosols were also carried out in the South Coast Air Basin as part of the CalNex project. A detailed description of the airborne measurements is given in Bahreini et al. (2012). Furthermore, measurements of POA composition and volatility taken at the Caldecott Tunnel in the San Francisco Bay Area reported in previous work (Worton et al., 2014) are also used to constrain the model as described below. The tunnel air samples were collected during July 2010.

Two additional datasets are used to evaluate the model. In addition to sampling ambient air, an aerosol mass spectrometer (AMS) sampled air that had been photochemically aged using an oxidation flow reactor (OFR) (Ortega et al., 2016). The OFR exposed ambient air to varying concentrations OH radicals in order to obtain photochemical ages much higher than the ambient levels observed at the Pasadena site, and the amount of SOA produced was quantified as a function of OH exposure. Moreover, radiocarbon (^{14}C) analysis has been performed on filter samples and results were combined with positive matrix factorization (PMF) data to determine fossil and

non-fossil fractions of the SOA components as reported in Zotter et al. (2014). The ^{14}C results are used for subsequent comparison against the box model from which fossil and non-fossil SOA mass can be estimated.

2.2 Model set-up

The SOA model is set-up to include 3 types of precursors: VOCs, P-IVOCs, and P-SVOCs. The parameters used in the box model to simulate the formation of SOA from these precursors are listed in Tables S1 to S3 of the supporting information. The box model dynamically calculates the evolution of organic species in an air parcel as it undergoes photochemical aging, hence producing SOA. The total SOA also includes background SOA (BG-SOA) at a constant concentration of $2.1 \mu\text{g m}^{-3}$, as determined in our previous work (Hayes et al., 2015). The model accounts for P-SVOC emissions from vehicular exhaust and cooking and treats POA as semi-volatile (Robinson et al., 2007). It should be noted that the model uses CO and NO_x as inputs to constrain the model, and the SOA yields for high- NO_x conditions are used, based on our previous work (Hayes et al., 2013; 2015). Therefore, to verify model performance both predictions of VOC and POA concentrations have been compared against field measurements and the model performance appears to be satisfactory (Hayes et al., 2015).

A schematic of the model is shown in Figure 1. All the model cases are listed in Table 1, and all the parameterizations are shown schematically in Figure 2. The first model case (ROB + TSI) incorporates the Robinson et al. (2007) parameterization for SOA formation that models P-IVOCs and P-SVOCs (i.e. P-S/IVOCs) using a single volatility distribution and oxidation rate constant. The ROB + TSI case also uses the Tsimpidi et al. (2010) parameterization for SOA formation from VOCs. A detailed description of the parameters used in ROB + TSI can be found in Hayes et al. (2015), and the ROB + TSI model case used here is identical to the case of the same name used in that paper. Briefly, as displayed in Fig. 2A, the Tsimpidi et al. (2010) parameterization proposes that the VOCs undergo an initial oxidation step that will form four lumped products with different volatilities ($c^* = 1, 10^1, 10^2, 10^3 \mu\text{g m}^{-3}$, where c^* is the effective saturation concentration). The first-generation oxidation products can be further oxidized, decreasing their volatility by one order of magnitude (i.e. aging). This “bin-hopping” mechanism repeats until the lowest volatility product is reached ($c^* = 10^{-1} \mu\text{g m}^{-3}$ in this study and $1 \mu\text{g m}^{-3}$ in other studies such as Tsimpidi et al. (2010) and Hayes et al. (2015). The Robinson et al. (2007) parameterization proposes that the P-S/IVOCs are initially distributed in logarithmically spaced volatility bins ranging from $c^* = 10^{-2}$ to $10^6 \mu\text{g m}^{-3}$. Thereafter, the oxidation of P-S/IVOCs decreases their volatility by one order of magnitude until the lowest volatility product is reached ($c^* = 10^{-2} \mu\text{g m}^{-3}$). The lowest volatility product possible is not the same for the oxidation of VOCs versus the oxidation of the P-S/IVOCs (10^{-1} vs. $10^{-2} \mu\text{g m}^{-3}$, respectively). However, whether the mass is

distributed into either bin has a negligible effect on the SOA mass simulated in the box model because of the relatively high SOA concentrations during the case study.

In this work, 5 model parameterizations are tested that incorporate new measurements of IVOCs and P-SVOC volatility as well as updated VOC yields that account for wall-losses of vapors (Zhang et al., 2014; Krechmer et al., 2016). For the first new case (ROB + ZHAO + TSI), we incorporate IVOC data measured in Pasadena during the CalNex campaign as reported from Zhao et al. (2014). In particular, the measured concentrations of speciated and unspeciated IVOCs and their estimated volatility are used to constrain the initial concentration of these species (as discussed in Section 2.2.2 below) as well as to estimate their yields (Zhao et al., 2014). Therefore, we replace the inferred concentrations of IVOCs that were used in our previous work and based on the volatility distribution of Robinson et al. (2007) with concentrations that are directly constrained by measurements. In the ROB + ZHAO + TSI case the SOA formation parameters used (e.g. yields, oxidation rate constants) are taken from Zhao et al. (2014) for the IVOCs and from Hayes et al. (2015) for the VOCs and SVOCs. Hodzic et al. (2016) have also estimated the IVOC yields while accounting for wall-losses using recent laboratory studies. However, the yields reported in that study are for a single lumped species, whereas in our work we estimate the yields using 40 IVOC categories, each representing a single compound or a group of compounds of similar structure and volatility. This method allows a more precise representation of IVOC yields and rate constants in the SOA model.

For the second new case (WOR + ZHAO + TSI), the volatility distribution of P-SVOCs is updated using measurements of POA performed at the Caldecott tunnel in the California Bay Area (Worton et al., 2014). In the previous two cases described above, the relative volatility distribution of P-SVOCs was taken from the work of Robinson et al. (2007). In this distribution, the relative concentration of SVOCs increases monotonically between the $c^* = 10^{-2}$ and $10^2 \mu\text{g m}^{-3}$ bins. The P-SVOC volatility distribution in the WOR + ZHAO + TSI case increases monotonically as well, but the relative concentrations in each bin are different and notably there is a much higher relative concentration of SVOCs in the $c^* = 10^2 \mu\text{g m}^{-3}$ bin (see Fig. 2 and Table S3 in the supporting information). In this model case, the updated P-SVOC volatility distribution is only applied to vehicular P-S/IVOCs whereas the volatility distribution proposed by Robinson et al. (2007) is still used for cooking emissions.

Several recently published papers have found that chamber experiments may underestimate SOA yields due to the loss of semi-volatile vapors to chamber walls (Matsunaga and Ziemann, 2010; Zhang et al., 2014; Krechmer et al., 2016). A sensitivity study has been performed to explore this uncertainty by running the three model cases described above (ROB + TSI, ROB + ZHAO + TSI, and WOR + ZHAO + TSI) with a revised version of the SOA yields for VOCs that accounts for these wall losses. A

detailed description of how these updated yields were estimated is provided in the supporting information and the values can be found in Table S4. Briefly, equilibrium partitioning is assumed to hold for the organic mass found in the gas phase, particle phase, or chamber walls. The SOA yields are then obtained by refitting SOA chamber yield curves using a model that accounts for partitioning between the three compartments (particle, gas, and wall) and incorporates the equivalent wall mass concentrations published in Krechmer et al. (2016), which are volatility dependent. The SOA chamber yield curves that were refitted were first calculated using the parameters published in Tsimpidi et al. (2010). There are limits to the assumption that partitioning between the three phases occurs on short enough timescales for all four VOC product volatilities that equilibrium is reached during an SOA chamber study. Specifically, at lower volatilities ($c^* \leq 1 \mu\text{g m}^{-3}$), the partitioning kinetics of the organic mass from the particles to the chamber walls have an effective timescale of more than an hour, which is similar or longer than typical chamber experiments (Ye et al., 2016). The limiting step in the partitioning kinetics is evaporation of SVOCs from the particles to the gas phase, and therefore the exact rate of evaporation depends on the OA concentration in the chamber.

Furthermore, as described in the supporting information, the updated SOA yields for VOC oxidation result in distribution of SVOC mass into lower volatility bins compared to the original parameterization, although the sum for the SVOC yields (α_i) remains similar. In the absence of aging, the SOA yields, Y , resulting from the wall-loss correction should be considered upper limits (MA parameterization), whereas the original yields serve as lower limits due to the considerations discussed above (TSI parameterization without aging). As shown in the supporting information (Figures S1 - S7) when aging (TSI parameterization with aging) is included the SOA yields increase beyond those observed when applying the wall loss correction for most of the VOC classes at longer photochemical ages. (It should be noted that SOA masses in Fig. S1 - S7 were calculated using the same background as for the other model cases, $2.1 \mu\text{g m}^{-3}$.) This feature of the aging parameterization is likely to blame for SOA over-predictions observed at long aging times when comparing with ambient data (e.g. Dzepina et al., 2009; Hayes et al., 2015).

According to Krechmer et al. (2016) and other chamber experiments (Matsunaga and Ziemann, 2010), the gas-wall equilibrium timescale doesn't vary strongly with the chamber size. The timescale for gas-wall equilibrium reported in these previous studies was 7 - 13 minutes. Similar timescales have been calculated for a variety of environmental chambers, including chambers that were used to determine many of the yields used in this paper. In addition, Matsunaga and Ziemann found that partitioning was nearly independent of chamber treatment, reversible, and obeyed Henry's law. Thus, the effective wall concentrations determined from the chamber experiments reported in Krechmer et al. (2016) are likely applicable to other chambers with different sizes.

The three model cases accounting for wall losses of organic vapors are named ROB + MA, ROB + ZHAO + MA, and WOR + ZHAO + MA. For these cases, the aging of the secondary SVOCs formed from the oxidation of VOCs was not included, since multi-generation oxidation is not well-constrained using data from chamber studies that are run over relatively short time-scales (i.e. hours). In addition, aging and correcting for wall-losses of organic vapors have been separately proposed to close the gap between observed and predicted SOA concentration from pre-2007 models, and are thought to represent the same “missing SOA mass.” Therefore, we run the model with one of these options at a time, as they are conceptually different representations of the same phenomenology. The aging of secondary SVOCs formed from the oxidation of P-IVOCs (and P-SVOCs) has been kept for all of the MA cases, however. To our knowledge, P-IVOC and P-SVOC mechanisms proposed in the literature have always included aging. A similar approach for correcting the yields as described above cannot be applied to P-IVOCs because organics with low volatilities ($c^* < 10 \mu\text{g m}^{-3}$) will partition to chamber walls very slowly, and SVOCs from P-IVOC oxidation tend to have lower volatilities than the SVOCs formed from VOC oxidation (Tables S1 and S2). Indeed, when trying to refit the VOC and IVOC yield curves, the model assuming equilibrium partitioning between particles, the gas phase, and the walls was able to reproduce the yield curves for VOCs, but not for IVOCs. This difference in the results is consistent with equilibrium not having been reached during the chamber studies on the IVOCs, which produce a greater amount of lower volatility SVOCs when compared to VOCs during oxidation. These lower volatility SVOCs have relatively slow evaporation rates from the particles, which prevents the chamber system from reaching equilibrium (Ye et al., 2016).

Simulations of O:C have been previously evaluated in Hayes et al. (2015) using laboratory and field data from CalNex to constrain the predicted O:C. It was concluded in that work that it was not possible to identify one parameterization that performed better than the other parameterizations evaluated, because of the lack of constraints on the different parameters used (e.g. oxidation rate constant, oxygen mass in the initial generation of products and that added in later oxidation generations, SOA yields, and emissions). Therefore, incorporating O:C predictions into the current box model and using those results in the evaluation discussed here would not provide useful additional constraints.

2.2.1 IVOC oxidation parameterizations

An important difference between the ROB + TSI and ROB + MA cases and the other four cases that have been updated with the IVOC measurements of Zhao et al. (2014) is that in the ZHAO cases, the first generation of IVOC oxidation distributes part of the product mass into four different volatility bins ($c^* = 10^{-1}, 1, 10^1, 10^2 \mu\text{g m}^{-3}$) as is displayed in Fig. 2E. This IVOC oxidation scheme is similar to that used for the first step

of VOC oxidation (Tsimpidi et al., 2010) as displayed in Fig. 2A and D, and has been used to model chamber measurements of SOA from IVOCs (Presto et al., 2010). Contrastingly, in the ROB + TSI and ROB + MA cases, a “bin-hopping” approach is used for all P-S/IVOCs where oxidation lowers volatility by only one order of magnitude (see Fig. 2B and C). The Robinson et al. (2007) parameters are still used for the formation of SOA from P-SVOCs in the ROB + ZHAO + TSI and ROB + ZHAO + MA cases, but the parameters are only applied to primary emissions in c^* bins between 10^{-2} and $10^2 \mu\text{g m}^{-3}$ inclusive (i.e. the volatilities corresponding to P-SVOCs).

2.2.2. Determination of initial precursor concentrations

In the ROB + TSI and ROB + MA cases, the initial concentration of P-S/IVOCs is estimated as follows. The volatility distribution determined by Robinson et al. (2007) is assumed to represent all P-S/IVOCs emitted (Dzepina et al., 2009). The total concentration of P-S/IVOCs is then set so that the amount of P-S/IVOCs in the particle phase is equal to the initial POA concentration. The initial POA concentration is determined from the product of the background-subtracted CO concentration and the $\Delta\text{POA}/\Delta\text{CO}$ emission ratio (Hayes et al., 2015). While this ratio may change due to evaporation/condensation or photochemical oxidation of POA, our previous work (Hayes et al., 2013) has shown that $\Delta\text{POA}/\Delta\text{CO}$ does not change significantly at the Pasadena ground site with observed photochemical age indicating that the ratio is insensitive to the extent of photochemical oxidation. Furthermore, it was calculated that the ratio would increase by 28% for an increase of OA concentration from 5 to $15 \mu\text{g m}^{-3}$, concentrations that are representative of this study. This possible source of error is substantially smaller than current errors suggested for P-S/IVOC emission inventories in 3-D models, where current schemes are based on scaling POA emission inventories with scaling factors that are not well constrained (Woody et al., 2016). The same method is used for the other four model cases, but only the initial concentration of P-SVOCs is estimated by this method and the initial concentration of P-IVOCs is estimated separately as described in the next paragraph. In addition, in the WOR + ZHAO + TSI and WOR + ZHAO + MA cases the volatility distribution of vehicular P-SVOCs reported in Worton et al. (2014) is used for estimating the initial concentration of vehicular P-SVOCs whereas the volatility distribution of Robinson et al. (2007) is used for estimating the initial concentration of cooking P-SVOCs.

It should be noted that the tunnel measurements do not include emissions due to cold starts of vehicles. In the box model, only the relative volatility distribution of vehicular POA measured during the tunnel study is used, and thus this potential source of error does not apply to the total amount of vehicular POA emissions in the model. However, it is still possible that the volatility distribution of POA is different during cold-starts compared to that of POA emitted from warm-running engines. To our knowledge,

measurements of the volatility distribution of POA during cold-starts are not available at this time. By comparing the SOA model results using two different POA volatility distributions (Robinson et al., 2007; Worton et al., 2014), we can evaluate to a certain extent the sensitivity of the simulated SOA concentration to the initial POA volatility distribution.

The initial concentrations of VOCs and IVOCs are calculated by multiplying the background-subtracted CO concentrations measured at Pasadena by the emission ratios $\Delta\text{VOC}/\Delta\text{CO}$ or $\Delta\text{IVOC}/\Delta\text{CO}$. In the ROB + TSI and ROB + MA cases this method is only applied to the VOCs. The initialization method for the concentrations of the VOCs is the same for all six cases in this paper. For the biogenic VOCs, we follow the same method as Hayes et al. (2015) to determine the initial concentrations since these compounds are not co-emitted with CO. The emission ratios are taken from the literature when available (Warneke et al., 2007; Borbon et al., 2013). For most of the IVOCs and some VOCs, emission ratios are not available in the literature. The ratios are instead determined by performing linear regression analyses on scatter plots of the IVOC or VOC and CO concentrations measured in Pasadena between 00:00-06:00 local time when the amount of photochemical aging was very low. During the regression analyses the x-intercept was fixed at 105 ppbv CO to account for the background concentration of CO determined in our previous work (Hayes et al., 2013). Thus, the slope of the resulting line corresponds to the estimated emission ratio ($\Delta\text{IVOC}/\Delta\text{CO}$).

It should be noted that the use of VOC emission ratios to CO to estimate VOC emissions does not assume that VOCs are always co-emitted with CO. Rather, it assumes that VOC emission sources are individually small and finely dispersed in an urban area, so that they are spatially intermingled with the sources of CO. Moreover, previous studies have measured the emission ratios of anthropogenic VOCs with respect to CO and the results show that vehicle exhaust is a major source of VOC and CO (Warneke et al., 2007; Borbon et al., 2013). Furthermore, the ratios are consistent both temporally and spatially. Thus, when thinking of the entire urban area as a source, the use of emission ratios to CO is justified. As shown in Hayes et al. (2015) in the supporting information, the modeled VOC concentrations are consistent with the measurements indicating that major VOCs sources have not been omitted, and the smooth time variations of the VOC concentrations support the use of a “global urban source”.

2.3 SOA model

The VOC yields are taken from Tsimpidi et al. (2010) or determined in this work as described below. The estimation of the IVOC yields (based on values taken from Presto et al. (2010) and of the OH reaction rate constants for IVOCs follows the same approach used by Zhao et al. (2014). However, instead of using the total SOA yield, Y , for a fixed OA concentration as reported in Zhao et al. (2014), we use the SVOC yield, α ,

of each c^* bin. It is important to note here that the SOA yields taken from Tsimpidi et al. and Presto et al. use a four-product basis set with $c^* = 10^0, 10^1, 10^2, 10^3 \mu\text{g m}^{-3}$ and $c^* = 10^{-1}, 10^0, 10^1, 10^2 \mu\text{g m}^{-3}$ respectively. For this box model, it is more appropriate to have a uniform VBS in terms of the bin range utilised so a bin with a lower volatility ($c^* = 10^{-1} \mu\text{g m}^{-3}$) has been added to the VBS distribution of Tsimpidi et al. (2010). The yield for bin $c^* = 10^{-1} \mu\text{g m}^{-3}$ is 0 for VOC oxidation, but when aging occurs mass can be transferred into this bin. However, the change in the total V-SOA mass is negligible because for both bin $c^* = 10^{-1}$ and $10^0 \mu\text{g m}^{-3}$ the secondary products almost completely partition to the particle phase.

The OH reaction rate constants are taken from the literature (Atkinson and Arey, 2003; Carter, 2010) as described previously in Hayes et al. (2015). During aging, the oxidation products undergo subsequent reactions with OH radicals with a reaction rate constant of $1 \times 10^{-11} \text{ cm}^3 \text{ molec}^{-1} \text{ s}^{-1}$ and $4 \times 10^{-11} \text{ cm}^3 \text{ molec}^{-1} \text{ s}^{-1}$ for the products of VOC oxidation and P-S/IVOC oxidation respectively (Hayes et al., 2015). For each oxidation step during aging, there is a mass increase of 7.5 % due to added oxygen.

The gas-particle partitioning is calculated in each bin by using the reformulation of Pankow theory by Donahue et al. (2006).

$$x_{p,i} = \left(1 + \frac{C_i}{C_{OA}}\right)^{-1}; C_{OA} = \sum_i [\text{SVOC}]_i x_{p,i}$$

Where $x_{p,i}$ is the particle phase fraction of lumped species i (expressed as a mass fraction); C_i is the effective saturation concentration, and C_{OA} is the total mass of organic aerosol available for partitioning (in $\mu\text{g m}^{-3}$). Only species in the gas phase are allowed to react with OH radicals in the model, since aerosol species react at much lower rates (Donahue et al., 2013).

The simulated SOA mass from the model is compared against field measurements of aerosol composition including results from PMF analysis of aerosol mass spectrometry data (Hayes et al., 2013; 2015). Specifically, the model predictions of urban SOA (i.e. SOA formed within the South Coast Air Basin) are compared against the semi-volatile oxygenated organic aerosol (SV-OOA) concentration from the PMF analysis. The other OA component also attributed to SOA, low-volatility oxygenated organic aerosol (LV-OOA), is primarily from precursors emitted outside the South Coast Air Basin and is used to estimate the background secondary organic aerosol (BG-SOA) as discussed previously (Hayes et al., 2015).

2.4 Correction for changes in partitioning due to emissions into a shallower boundary layer upwind of Pasadena

As described in Hayes et al. (2015), during the transport of the pollutants to Pasadena, the planetary boundary layer (PBL) heights increase during the day. Using CO as a conservative tracer of emissions does not account for how the shallow boundary layer over Los Angeles in the morning influences gas-particle partitioning due to lower vertical mixing and higher absolute POA and SOA concentrations at that time. Thus, as shown in the gas-particle partitioning equation above, there will be a higher partitioning of the species to the particle phase and less gas-phase oxidation of primary and secondary SVOCs. Later in the morning and into the afternoon the PBL height increases (Hayes et al., 2013) diluting the POA and urban SOA mass as photochemical ages increases. However this is a relatively small effect as the partitioning calculation in the SOA model is relatively insensitive to this effect and the absolute OA concentrations (Dzepina et al., 2009; Hayes et al., 2015). Our previous work (Hayes et al., 2015) found in a sensitivity study a +4/-12% variation in predicted urban SOA when various limiting cases were explored for simulation of the PBL (e.g. immediate dilution to the maximum PBL height measured in Pasadena versus a gradual increase during the morning).

To account for the effect of absolute OA mass on the partitioning calculation, the absolute partitioning mass is corrected using the following method. A PBL height of 345 m is used for a photochemical age of 0 h and it reaches a height 855 m at a photochemical age of 9.2 h, which is the maximum age for the ambient field data. Between the two points, the PBL is assumed to increase linearly. The boundary layer heights are determined using ceilometer measurements from Pasadena at 6:00 - 9:00 and 12:00 - 15:00 local time, respectively (Hayes et al., 2013). The second period is chosen because it corresponds to when the maximum photochemical age is observed at the site. The first period is chosen based on transport times calculated for the plume from downtown Los Angeles (Washenfelter et al., 2011) that arrives in Pasadena during the afternoon. There are certain limitations to this correction for the partitioning calculation. First, the correction is based on a conceptual framework in which a plume is emitted and then transported to Pasadena without further addition of POA or SOA precursors. A second limitation is that we do not account for further dilution that may occur as the plume is advected downwind of Pasadena. However, such dilution is not pertinent to the OFR measurements, and so for photochemical ages beyond ambient levels observed at Pasadena, we focus our analysis on the comparison with the OFR measurements.

3. RESULTS AND DISCUSSION

3.1 Evolution of SOA concentration over 3 days

We follow an approach similar to Hayes et al. (2015) in order to analyse the model results. The model SOA concentration is normalized to the background subtracted CO concentration to account for dilution, and the ratio is then plotted against photochemical age rather than time to remove variations due to diurnal cycles of precursor and oxidant concentrations. The photochemical age is calculated at a reference OH radical concentration of $1.5 \times 10^6 \text{ molec cm}^{-3}$ (DeCarlo et al., 2010). Figure 3 shows this analysis for each model case for up to 3 days of photochemical aging. Since fragmentation and dry deposition are not included in the model, it has only been run to 3 days in order to minimize the importance of these processes with respect to SOA concentrations (Ortega et al., 2016). Nevertheless, it is very likely that gas-phase fragmentation of SVOCs (e.g. branching between functionalization and fragmentation) occurs during oxidative aging over these photochemical ages as is discussed in further detail below.

In each panel of Fig. 3, field measurements are included for comparison. The ambient urban SOA mass at the Pasadena ground site is generally measured under conditions corresponding to photochemical ages of 0.5 days or less (Hayes et al., 2013). The airborne observations of SOA in the Los Angeles basin outflow are also shown as the average of all data between 1 and 2 days of photochemical aging (Bahreini et al., 2012). The gray region on the right serves as an estimate for very aged urban SOA based on data reported by de Gouw and Jimenez (2009). The data from the OFR and a fit of the ambient and reactor data (dotted black line) are also displayed in Fig. 3 (Ortega et al., 2016). In addition, Figure 4 shows the ratio of modeled-to-measured SOA mass on a logarithmic axis to facilitate evaluation of model performance.

As displayed in the graphs for Fig. 3, it should be noted the measurements from the OFR (Ortega et al., 2016) and from the NOAA P3 research aircraft (Bahreini et al., 2012) give quite similar results for SOA/ Δ CO. The OFR measurements are not affected by particle deposition that would occur in the atmosphere at long timescales or photochemical ages. Only a few percent of the particles are lost to the walls of the reactor, and this process has been corrected for already in the results of Ortega et al. The similarity in the two types of observations suggests that ambient particle deposition and plume dispersion do not significantly change the SOA/ Δ CO ratio over the photochemical ages analyzed here.

In ROB + TSI, as described in previous work (Hayes et al., 2015), there is a large over-prediction of SOA mass at longer photochemical ages. As displayed in Fig. 3, the amount of SOA produced in the model is higher than all of the field measurements taken

at a photochemical age longer than 0.5 days. Moreover, the ratios of model to measurement are higher than the upper limit of the gray bar representing the ratios within the measurement uncertainties. There is an agreement with the measurements at moderate photochemical ages (between 0.25 and 0.50 days), but the SOA mass simulated by the model is slightly lower than the measurements at the shortest photochemical ages (less than 0.25 days) even when accounting for measurement uncertainties. In this parameterization, most of the SOA produced comes from the P-S/IVOCs, and uncertainties in the model with respect to these compounds likely explain the overestimation observed at longer photochemical ages. As discussed in the introduction, a major goal in this work is to better constrain the amount of SOA formed from the oxidation of P-S/IVOCs, and the following two model cases (ROB + ZHAO + TSI and WOR + ZHAO + TSI) seek to incorporate new measurements to better constrain the box model with respect to the P-S/IVOCs.

When the yield, rate constants, and initial concentrations of P-IVOCs are constrained using the field measurements reported in Zhao et al. (2014) (ROB + ZHAO + TSI), the SOA mass simulated by the model shows much better agreement with the measurements at longer photochemical ages (Fig. 3 and 4). There is a slight over-prediction at 2 days of photochemical aging, but the model is still within the range of measurements of very aged urban SOA reported by De Gouw and Jimenez (2009). The parameterization reported in Robinson et al. (2007) for P-S/IVOCs is based on one study of the photo-oxidation of diesel emissions from a generator (Robinson et al., 2007). The results obtained here for the better constrained ROB + ZHAO + TSI case indicate that the initial concentrations of P-IVOCs as well as the P-IVOC yields within ROB + TSI are too high which leads to over-prediction of SOA concentration at longer photochemical ages. On the other hand, the SOA mass simulated in ROB + ZHAO + TSI is biased low at shorter photochemical ages (less than 1 day). Similar to other recent studies (Gentner et al., 2012; Hayes et al., 2015; Ortega et al., 2016), there may be unexplained SOA precursors not included in the model which rapidly form SOA or yields for fast-reacting species including certain VOCs may be biased low. Both of these possibilities are explored in the other model cases discussed below.

The WOR + ZHAO + TSI case simulates higher SOA concentrations at shorter photochemical ages compared to the previous case (ROB + ZHAO + TSI), but it is still biased low at shorter photochemical ages. The more rapid SOA formation is due to the updated SVOC volatility distribution in this model case compared to the cases that use the Robinson et al. (2007) distribution. Specifically, as shown in Fig. 2F, there is a higher relative concentration of gas phase SVOCs in the $c^* = 10^2$ bin and thus a higher ratio of P-SVOC to POA. Given that in the box model (and in most air quality models) the P-SVOC emissions are determined by scaling the POA emissions according to their volatility distribution, a higher P-SVOC to POA ratio will then result in a higher initial P-

SVOCs concentration. Furthermore, SOA formation from P-SVOCs is relatively fast. Together these changes lead to increases in SOA formation during the first hours of photochemical aging when using the Worton et al. volatility distribution. This case suggests that P-SVOCs in their highest volatility bin ($c^* = 10^2 \mu\text{g m}^{-3}$ bin) that are emitted by motor vehicles may be responsible for some of the observed rapid SOA formation within the South Coast Air Basin. When observing the SOA mass simulated at photochemical ages higher than 1 day, the simulation is similar to ROB + ZHAO + TSI. There is better model/measurement agreement than for the ROB + TSI case, but a small over-prediction is observed in the comparison to the reactor data at 2 days of photochemical aging.

Also shown in the right-hand panels of Fig. 3 and 4 are the results with the updated yields for the VOCs that account for gas phase chamber wall losses. For these last three cases (ROB + MA, ROB + ZHAO + MA, and WOR + ZHAO + MA), the rate of SOA formation at short photochemical ages is faster because the secondary SVOC mass from the oxidation of the VOC precursors is distributed into lower volatility bins compared to the Tsimpidi et al. (2010) parameterization. In the ROB + MA case (Fig. 3D and 4D), similar to ROB + TSI, an over-prediction is obtained at longer photochemical ages. There is an improvement in the model at the shortest photochemical ages, but the simulated mass is still lower than the measurements even when considering the measurement uncertainty. Both of these cases perform less well for SOA formation within the South Coast Air Basin, and therefore the remainder of this study is focused on the other four model cases. Overall, the model cases using the updated yields for V-SOA show improvement for the shorter photochemical ages, and the evolution of SOA concentration as a function of photochemical age better corresponds to the various measurements taken at Pasadena and from the OFR.

Specifically, the ROB + ZHAO + MA and the WOR + ZHAO + MA cases both better represent SOA formation and exhibit better model/measurement agreement among the different cases used in this work. They are both consistent with the OFR reactor data at longer photochemical ages as shown in Figs. 3 and 4 compared with the other cases. At a qualitative level, the MA parameterization simulations are more consistent with the fit of the OFR measurements in which the SOA mass remains nearly constant at longer photochemical ages. In contrast, the cases with the TSI parameterization do not follow this trend as the SOA mass keeps increasing between 2 and 3 days age, which is not observed in the measurements. As already mentioned, the model used for this work does not include fragmentation reactions, and including these reactions, in particular branching between functionalization and fragmentation during gas-phase SVOC oxidation, may improve the cases using a potential update of the TSI parameterization as discussed below. Fig. 4F indicates that including additional P-SVOC mass in the model and accounting for gas-phase wall losses in chamber studies improves SOA mass

concentration simulations with respect to the measurements. However, in the WOR + ZHAO + MA case there is still a slight under-prediction of SOA formed at shorter photochemical ages (between 0.05 and 0.5 days), and this discrepancy is observed in all the other model cases. Given the uncertainties in the model set-up discussed in the experimental section, it is not possible to conclude if one of the four cases (i.e. ROB + ZHAO + TSI, WOR + ZHAO + TSI, ROB + ZHAO + MA, WOR + ZHAO + MA) more accurately represents SOA formation in the atmosphere.

According to the OFR data from Ortega et al. (2016), the mass of OA starts to decay due to fragmentation after heterogeneous oxidation at approximately 10 days of photochemical aging. The results are consistent with other OFR field measurements (George and Abbatt, 2010; Hu et al., 2016; Palm et al., 2016). In this work, the model is run only up to 3 days, which is much shorter than the age when heterogeneous oxidation appears to become important. In fact, when including a fragmentation pathway for each of the model cases, a reduction of OA of only 6 % is observed compared to the cases without fragmentation at 3 days of photochemical aging. In this sensitivity study, the fragmentation is parameterized as an exponential decrease in OA concentration that has a lifetime of 50 days following Ortega et al. (2016). Given the results, the inclusion of fragmentation due to heterogeneous oxidation in the model does not significantly change the model results or the conclusions made in this work.

More generally, there are at least three different fragmentation mechanisms that could be responsible for the decrease of SOA formation at very high photochemical ages. The first mechanism is the reaction of oxidants (e.g. OH) with the surface of an aerosol particle and decomposition to form products with higher volatility, i.e., due to the heterogeneous oxidation just described. The second type of fragmentation that may be important for very high photochemical ages in the OFR is due to the high concentration of OH (Palm et al., 2016). Most of the molecules in the gas phase will react multiple times with the available oxidants before having a chance to condense, which will lead to the formation of smaller products too volatile to form SOA. However, this is only important at very high photochemical ages in the OFR, which are not used in this work. A third type of fragmentation can occur during the aging of gas-phase SVOCs (Shrivastava et al., 2013; 2015). The TSI parameterization used in the model from this work and from previous modeling works (Robinson et al., 2007; Hodzic et al., 2010; Shrivastava et al., 2011) only includes the functionalization of the SVOCs and neglects fragmentation reactions. More recently, Shrivastava et al. (2013) have modified the VBS approach in a box model by incorporating both pathways and performed several sensitivity studies. The results when including fragmentation generally exhibit better agreement with field observations, but as noted in that work the agreement may be fortuitous given that both the emissions as well as the parameters representing oxidation in the model are uncertain. This third type of fragmentation is not simulated in our

sensitivity study using the approach above, and it remains poorly characterized due to the complexity of the chemical pathways and the number of compounds contributing to SOA formation as described in Shrivastava et al. (2013).

Despite having higher SOA yields initially, over regional scales (i.e. photochemical ages at and above approximately 2 days) the parameterizations with updated V-SOA yields and without aging produce less SOA, because the organic mass in higher volatility bins ($c^* = 100$ and $1000 \mu\text{g m}^{-3}$) is not further oxidized by aging reactions to produce organics with sufficiently low volatilities to form SOA (Fig. S1 – S7). Furthermore, large SOA overpredictions have been shown to occur in gridded 3-D models when using parameterizations with aging that do not include fragmentation reactions (Shrivastava et al., 2015). Fragmentation with aging reactions may still play a role in determining SOA concentrations on such regional scales. However for the photochemical ages studied here, our results as well as the recent findings regarding gas-phase wall losses in chamber studies, suggest the inclusion of updated V-SOA yields as well as accurate parameterizations for I-SOA and S-SOA and for the emissions of precursors is more important for accurately predicting urban SOA concentrations.

Finally, Woody et al. (2016) recently proposed a meat cooking volatility distribution and therefore we perform a sensitivity study by using this distribution in our model for P-SVOCs coming from cooking sources. The results are displayed in the supporting information (Figure S8), where this alternate approach has been implemented for the WOR + ZHAO + TSI and WOR + ZHAO + MA cases. By comparing the results obtained from this sensitivity study with Fig. 3, the two cases in the sensitivity study display a slight decrease of SOA/ ΔCO values over 3 days of photochemical aging with a difference of approximately 9 % at 3 days. Thus, the model-measurement comparison does not change significantly relative to the base case. Given the similarities between the sensitivity study and Fig. 3, as well as the possibility of cooking SOA sources other than meat-cooking (i.e. heated cooking oils, Liu et al. (2017)), the remainder of our work uses the Robinson et al. volatility distribution for P-SVOCs from cooking sources.

3.1.1 SOA concentration estimated at Pasadena: fossil and non-fossil fractions

In the top panel of Figure 5, the box model is compared against the urban SOA determined by PMF analysis of the AMS measurements at Pasadena (Hayes et al., 2013). In the bottom panel of the same figure the model is compared against the fossil and non-fossil fraction of urban SOA as obtained from ^{14}C measurements reported in Zotter et al. (2014). Both panels show measurements and predictions corresponding to 12:00 – 15:00 local time, when SOA concentrations peaked due to longer photochemical ages (5 hours on average) as well as the arrival of emissions transported from source-rich western regions of the South Coast Air Basin.

Similar to the results in Fig. 3 and 4 for short photochemical ages, the SOA mass simulated by the ROB + ZHAO + TSI case is biased low in Fig. 5A. The ROB + ZHAO + MA, WOR + ZHAO + TSI, and WOR + ZHAO + MA cases show better model/measurement agreement as the simulated SOA mass is within the measurement uncertainty or essentially equal to the lower limit of the concentration that is defined by the measurement uncertainty. Fig. 5A also allows evaluation of the contribution of each precursor type to the SOA at Pasadena. For the four cases displayed, the P-SVOCs and P-IVOCs are responsible for 70 – 83 % of the urban SOA formation. Thus, more than half of the urban SOA is attributed to these precursors even in the MA parameterizations where the model is run with the updated yields, which doubles V-SOA compared to the cases using the yields reported from Tsimpidi et al. (2010). Furthermore, 8 – 27 % of the measured urban SOA is due to V-SOA where the range of values is due to the uncertainty in the measurements as well as the difference in simulated V-SOA concentration for each case.

According to the ^{14}C measurements, an average of 71 ± 3 % of urban SOA at Pasadena is fossil carbon, which is thought to be due to the importance of vehicular emissions, especially during the morning rush hour (Bahreini et al., 2012; Zotter et al., 2014; Hayes et al., 2015). In general, the box model gives results consistent with the ^{14}C measurements. To make this comparison, the simulated SOA is apportioned between fossil S-SOA, fossil I-SOA, fossil V-SOA, cooking S-SOA, and biogenic V-SOA. The last two apportionments correspond to non-fossil carbon. This evaluation is possible following an approach similar to Hayes et al. (2015) where the identity of the precursor is used to apportion SOA. Briefly, the fossil S-SOA is formed from P-SVOCs emitted with hydrocarbon-like OA (HOA), which is a surrogate for vehicular POA. Second, cooking S-SOA is formed from P-SVOCs emitted with cooking-influenced OA (CIOA). The concentrations of HOA and CIOA were determined previously using PMF analysis. Fossil V-SOA is formed from aromatics, alkanes, and olefins while isoprene and terpenes are responsible for biogenic V-SOA. The treatment of IVOCs in the comparison with the ^{14}C measurements has been updated from our 2015 study. Previously, it was assumed that P-IVOCs were co-emitted with cooking-influenced OA, but the recent work of Zhao et al. (2014) and others indicates that petroleum sources contribute substantially to IVOC emissions (Dunmore et al., 2015; Ots et al., 2016). Therefore, the IVOCs are considered entirely fossil carbon in order to obtain the results shown in Fig. 5B.

As seen in Fig. 5B, for all the model cases, cooking S-SOA dominates the non-fossil fraction and biogenic VOCs have only a small contribution to non-fossil urban SOA. This result is consistent with our previous work, and indicates agreement between the model and ^{14}C measurements cannot be achieved without including an urban source of non-fossil carbon such as P-SVOCs from cooking. With respect to fossil SOA, more S-SOA is formed when using the volatility distribution of vehicular POA reported from

Worton et al. (2014) due to the greater proportion of gas-phase of P-SVOCs. When the V-SOA yields are updated in the model (MA parameterizations), there is a corresponding increase in both fossil and non-fossil V-SOA.

When comparing the fossil/non-fossil carbon split, all the cases are either in agreement with the measurement within its uncertainty, or slightly lower. Starting with the ROB + ZHAO + TSI case, the fossil fraction increases from 75 % to 79 % in each case as VOCs or P-SVOCs from vehicle emissions have greater importance for SOA formation. While the uncertainties reported in Zotter et al. (2014) were 71 ± 3 %, there are likely additional errors due to different factors that may influence the model or measurements. For example, a portion of the P-IVOCs may be from cooking sources rather than entirely from fossil sources as is assumed above (Klein et al., 2016). Taking the WOR + ZHAO + MA case as an example, since it is the best performing case in this work according to Fig. 5A, model/measurement agreement is obtained within measurement uncertainties if one assumes that 19 – 39 % of P-IVOCs come from cooking emissions. Ultimately, the differences observed in the comparison with the ^{14}C data are very likely smaller than these errors discussed here, and it is concluded that all the model cases perform equally well with respect to the fossil/non-fossil carbon split.

As reported in Gentner et al. (2012), emissions from petroleum derived fuels such as diesel and gasoline have an important contribution to the formation of SOA. However, there have been conflicting results regarding the relative contributions of diesel versus gasoline emissions (Bahreini et al., 2012; Gentner et al., 2012). In this work, the relative contribution of different SOA sources is estimated following a procedure similar to that previously published in Hayes et al. (2015), and the results are shown in Figure S9 of the supporting information. Briefly, the source apportionment method follows four steps. First, after classifying the SOA mass from isoprene and terpenes as biogenic V-SOA, the remaining V-SOA is attributed to gasoline emissions since the diesel contribution to V-SOA is small (~ 3 %) (Hayes et al., 2015). Second, for the diesel and gasoline contribution to S-SOA, 70(± 10) % of HOA is emitted from diesel vehicles with the remainder from gasoline vehicles (Hayes et al., 2013), and thus it is assumed for the source apportionment that 70% (30%) of vehicular P-SVOCs are from diesel (gasoline) vehicles. Third, the S-SOA from cooking sources is calculated separately in the model, where the initial concentration of cooking P-SVOCs is estimated using the measured CIOA concentration and the method described in Section 2.2.2 above. Lastly, the fractional contributions to I-SOA mass is difficult to determine since there are still uncertainties about the sources of IVOCs. According to Zhao et al. (2014), petroleum sources other than on-road vehicles likely contribute substantially to primary IVOCs, but evidence exists that cooking may be a source of IVOCs as well (Klein et al., 2016). Thus, while we attribute I-SOA to these two sources, we do not distinguish the sources. The estimated source apportionment in Fig. S9 attributes urban SOA as follows: 4% to

biogenic V-SOA, 22% to gasoline V-SOA, 9% to gasoline S-SOA, 20 % to diesel S-SOA, and 16 % to cooking S-SOA. The remaining 29 % is I-SOA that is either due to cooking or off-road emissions of P-IVOCs.

It should be noted that according to McDonald et al. (2015), the emissions from vehicles have decreased over time (i.e. between 1970 and 2010) due to regulations in California. Warneke et al. (2012) have observed also that the emission ratios of some SOA precursors (i.e. $\Delta\text{VOC}/\Delta\text{CO}$) have remained constant between 2002 and 2010, while absolute concentrations have decreased. On the other hand, cooking and off-road emissions are subject to different regulations in California, and the ratios of cooking or off-road emissions to vehicular emissions have likely changed with time, which means that the source apportionment results for urban SOA presented here will be specific to 2010.

3.2 SOA formation versus precursor oxidation rate constant

Recent results from Ortega et al. (2016) point to the importance of fast-reacting precursors for urban SOA during CalNex, and we can use their results to further evaluate our box model. The fraction of SOA formed from each precursor class as a function of the precursor rate constant is displayed in Figure 6. The right-axis of Fig. 6 shows the correlation (R^2) of different VOCs with the maximum concentration of SOA formed using the OFR as a function of their oxidation rate constants as reported in Ortega et al. (2016). This analysis of the OFR data allows us to constrain the rate constants of the most important SOA precursors. A detailed description of how the R^2 values were obtained can be found in Ortega et al. (2016). According to the R^2 data, the VOC compounds that correlate best with maximum SOA formation potential are those that have $\log k_{\text{OH}}$ rate constants ranging from -10.5 to -10.0. When comparing the percentage of SOA mass simulated by the model with the observed R^2 values, all of the four cases are not entirely consistent with the R^2 data. According to the model, more SOA mass is formed from precursors in the bin ranging from -11.0 to -10.5 (the majority of mass formed comes from P-IVOCs) rather than the bin ranging from -10.5 to -10.0. In contrast, the R^2 value is higher for the more reactive bin. If either fast-reacting precursors were missing in the model, or if the rate constants of the currently-implemented precursors were too small, then correcting either error would shift the relative distribution shown in Fig. 6 towards faster-reacting SOA precursors. In turn, the trend in the percentage of modeled SOA mass may more closely follow the trend in R^2 values.

3.3 Volatility distribution of OA

Based on the evaluations carried out up to this point on the six model cases, the WOR + ZHAO + MA case seems to most closely reproduce the observations. Thus, the entire volatility distribution of the OA, precursors, and secondary gas phase organics is analyzed for this model case. Figure 7 shows this distribution for three selected photochemical ages: 0, 5, and 36 h. The figure allows us to track the evolution of SOA and secondary gas phase organics from each precursor class in terms of their concentration and volatility and also to evaluate the reduction of precursor concentrations. For the model results, the volatility distribution of all organics resolved by precursor class, except for the VOCs and P-IVOCs, can be taken directly from the model. To determine the volatility distribution of the VOCs and P-IVOCs, the SIMPOL.1 method (Pankow and Asher, 2008) is used to estimate the effective saturation concentration of each compound or lumped species in the model. Also included in Fig. 7, in the bottom-right panel, is the observed volatility distribution for the Pasadena ground site, which is an average of measurements collected during 12:00 – 15:00 local time and corresponds to 5 h of photochemical aging. For the measurements, the volatility distribution of VOCs was determined using GC-MS data (Borbon et al., 2013) whereas the IVOC distribution is taken from Zhao et al. (2014). The volatility distribution of SVOCs was determined using combined thermal denuder AMS measurements (see the supporting information for further details).

For the volatility distribution of the model at time 0, the concentrations of P-SVOCs and P-IVOCs monotonically increases with the value of c^* . However, a discontinuity in the mass concentration exists between the $c^* = 10^2$ and $10^3 \mu\text{g m}^{-3}$ bins. This discontinuity can be explained by several factors. First, the measured IVOCs mass concentration the $c^* = 10^3 \mu\text{g m}^{-3}$ bin is very low, and since the initial concentrations of IVOCs in the model are constrained by the field measurements, the model will also have very low concentrations. Zhao et al. (2014) have already noted that the concentration of P-IVOCs in this bin is relatively low when compared to the volatility distribution from Robinson et al. (2007). Another possible explanation is the presence of cooking sources, which in the model are responsible for substantial P-SVOC mass (~50%) but may have a smaller contribution to the P-IVOC mass.

During oxidation the volatility distribution evolves and the concentration of secondary organics increases in the bins between $c^* = 10^{-1}$ and $10^3 \mu\text{g m}^{-3}$ (inclusive), and the largest portion of SOA is found in the $c^* = 1 \mu\text{g m}^{-3}$ bin. This result is due to the partitioning of the organic mass to the particle phase and the lack of particle phase reactions in the model, which leads to very slow oxidation rates for species found in the lower volatility bins. After 36 h, a large portion of the precursors have been reacted,

although some primary and secondary material remains in the gas phase giving rise to more gradual SOA formation.

In Fig. 7, it is possible to compare the measured volatility distribution with the model simulation at 5 h of photochemical aging. It should be noted that the relatively high concentrations of VOCs in the model compared to the measurements are due to the model containing VOCs for which measurements were not obtained in Pasadena. There are 47 VOCs used in the model and only 19 VOCs were measured. However, the remaining VOCs have been measured in other urban locations (Warneke et al., 2007; Borbon et al., 2013) and thus it is assumed they are also present in the South Coast Air Basin. For this work, we include these 28 remaining VOCs by assuming that they are also emitted in the South Coast Air Basin with identical emission ratios ($\Delta\text{VOC}/\Delta\text{CO}$). When comparing only VOCs measured and modeled (shown in hollow black bars), the results are consistent (3.1, 3.6 and 2.2 $\mu\text{g m}^{-3}$ from $c^* = 10^7$ to $10^9 \mu\text{g m}^{-3}$ bins versus 3.8, 3.7 and 2.2 $\mu\text{g m}^{-3}$ for the measurements). On the other hand, the model appears to have a low bias for the concentrations of P-IVOCs (0.16, 0.63, 0.89 and 2.3 $\mu\text{g m}^{-3}$ from $c^* = 10^3$ to $10^6 \mu\text{g m}^{-3}$ bins versus 0.21, 1.39, 2.65 and 3.82 $\mu\text{g m}^{-3}$ for the measurements). This low bias is seen for each volatility bin and could possibly be explained by either oxidation rate constants that are too high or $\Delta\text{IVOC}/\Delta\text{CO}$ ratios that are too low. The latter explanation seems more likely given that the rate constants estimated using surrogate compounds and structure-activity relationships for the unspiciated P-IVOCs are generally lower limits (Zhao et al., 2014), which would result in a high bias rather than a low bias. The $\Delta\text{IVOC}/\Delta\text{CO}$ ratios may be low because the photochemical age between 00:00 – 6:00 local time is not strictly zero, and some oxidation may have occurred during the period used to determine the ratio values. Emission ratios such as $\Delta\text{IVOC}/\Delta\text{CO}$ facilitate incorporating P-IVOC emissions into 3-D models that already use CO emissions inventories, and the $\Delta\text{IVOC}/\Delta\text{CO}$ ratios reported here could be used for this purpose. However, the resulting I-SOA concentrations should be considered lower limits given that the emission ratios, and also the rate constants, are likely themselves lower limits.

To further explore the impact of potential errors in the initial IVOC concentrations, a sensitivity study has been carried out using initial concentrations calculated based on the observed photochemical age and measured IVOC concentrations at Pasadena as well as the estimated IVOC oxidation rate constants (Zhao et al., 2014). This alternate approach is implemented for the ROB + ZHAO + MA and WOR + ZHAO + MA cases and does not use nighttime IVOC-to-CO ratios. The results when using this alternative approach are shown in the supporting information (Figure S10). When comparing Fig. S10 with Fig. 3, differences are minor. The model/measurement agreement improves slightly at shorter photochemical ages (less than 1 day). At the same time a slightly larger over-prediction is observed at longer photochemical ages. However,

the formation of SOA modeled in this sensitivity test is similar to the original cases from Fig. 3 with an average difference of only 21 %, which represent a relatively small error compared to other uncertainties in SOA modeling. The IVOC initial concentrations used in this sensitivity test are slightly higher than those calculated using the IVOC-to-CO ratio, which explain the small increase of modeled SOA/ Δ CO. Ultimately, the different approaches for determining the initial IVOC concentration in the model are reasonably consistent, and both approaches perform similarly given the model and measurement uncertainties.

For the measurements of SVOCs, all the mass in bins lower than $10^{-2} \mu\text{g m}^{-3}$ are lumped into this bin for Fig. 7 since the model does not contain lower volatility bins. In addition, the 10^1 and $10^2 \mu\text{g m}^{-3}$ bins are not well-resolved because the thermal denuder did not consistently reach temperatures low enough (less than 37°C) to resolve SVOCs in this range of volatilities. Thus, the $10^1 \mu\text{g m}^{-3}$ bin may contain some higher volatility particulate mass although this contribution is expected to be small due to the low particle phase fraction of compounds in the $10^2 \mu\text{g m}^{-3}$ bin. With these considerations in mind, the volatility distribution of the SVOCs is somewhat different in the model compared to the measurements. Most notably, the model does not form a significant amount of lower volatility SOA in the $10^{-2} \mu\text{g m}^{-3}$ bin, whereas the measurements have a much higher concentrations in this bin. A factor that may explain this difference between the volatility distributions is the lack of particle phase reactions that continue to transform SOA into lower volatility products, a process which is not considered in the model. One example of a particle phase reaction is the formation of SOA within deliquesced particles, including the partitioning of glyoxal to the aqueous phase to produce oligomers as discussed in Ervens and Volkamer (2010), although that specific mechanism was of little significance during CalNex (Washenfelder et al., 2011; Knote et al., 2014). Alternatively, the use of an aging parameterization where the volatility may decrease by more than one order of magnitude per oxidation reaction would also distribute some SOA mass into lower c^* bins. Hayes et al. (2015) previously evaluated different parameters for aging. However, the results from this previous study showed that substantial over-prediction of SOA was observed when using the Grieshop et al. (2009) parameterization in which each oxidation reaction reduced volatility by two orders of magnitude. New parameterizations may be necessary to produce the observed SOA volatility and concentration simultaneously (Cappa and Wilson, 2012). However, we note that the additional low volatility organic mass will not significantly change SOA predictions in urban regions where OA concentrations are relatively high. When comparing the total amount of particle phase SVOCs, it seems that the model reproduces reasonably well the measurements (6.2 versus $9.0 \mu\text{g m}^{-3}$) as expected based on the comparisons of the total SOA concentration discussed above. In addition, the total amount of SVOCs (particle and gas phase) are similar (11.2 vs $11.8 \mu\text{g m}^{-3}$), although it is difficult to determine from measurements the

gas phase concentration of SVOCs in the $10^2 \mu\text{g m}^{-3}$ bin due to the lack of particle mass in this bin under ambient concentrations as well as the limited temperature range of the thermal denuder system.

Recently, Woody et al. (2016) published a paper that modeled SOA over California using the Environmental Protection Agency's Community Multiscale Air Quality Model that had been updated to include a VBS treatment of SOA (CMAQ-VBS). As discussed in that paper, the modeled P-S/IVOC emission inventories remain an important source of uncertainty in 3-D grid-based models. In that previous study several different ratios of P-S/IVOCs-to-POA emissions were evaluated against measurements, and it was found that a ratio of 7.5 gave the best agreement between the CMAQ-VBS model and observations. From the results shown in Fig. 7 at a photochemical age of 0 h, a P-S/IVOC-to-POA ratio of 5.2 is calculated. This ratio is different from that determined by Woody et al. (2016), and may be biased low due to possibly low $\Delta\text{IVOC}/\Delta\text{CO}$ emission ratios as discussed earlier in this section, but it serves as both a useful lower bound and has the advantage of being determined from empirical measurements of aerosols rather than by tuning a model to match measured SOA concentrations. As stated in Woody et al. (2016), the higher ratio may compensate for other missing (or underrepresented) formation pathways in SOA models or excessive dispersion of SOA in their model.

4. CONCLUSION

We have used several data sets from recently published papers to better constrain and evaluate urban SOA formation pathways and precursors, especially P-SVOCs and P-IVOCs, within a custom-built box model. The use of the box model facilitates the incorporation of these new data sets as well as the evaluation of a number of model cases. All the model cases are able to correctly simulate the fossil/non-fossil carbon split at the Pasadena ground site providing support for the performance of the model. When measurements of IVOCs are used to constrain the concentrations of P-IVOCs, such as in the ROB + ZHAO + TSI and ROB + ZHAO + MA cases, a large improvement of the model at longer photochemical age is observed. However, these model cases are still biased low at shorter photochemical ages. By constraining the P-SVOCs additionally with measurements of those precursors, such as in the WOR + ZHAO + TSI case, better model/measurement agreement is obtained at shorter photochemical ages, yet the model is still biased low. Finally, the WOR + ZHAO + MA case, which incorporates state-of-the-art measurements of P-SVOCs and P-IVOCs and also accounts for the effect of chamber wall-losses on VOC yields, obtains model/measurement agreement within measurement uncertainties at long photochemical ages. Although, it displays also a low bias at short photochemical ages, which is similar to the ROB + ZHAO + MA case. This bias may be due to low $\Delta\text{IVOC}/\Delta\text{CO}$ emissions ratios or IVOC oxidation rate constants

for which the estimated values are too low. It is also possible that additional sources or SOA formation pathways are missing from the model. Moreover, a P-S/IVOC-to-POA ratio of 5.2 is determined, which can be combined with POA emission inventories to constrain the emissions of P-S/IVOCs in gridded chemical transport models.

In addition to evaluating the model performance with respect to SOA concentration, the rates of SOA formation are compared against measurements as well. This aspect of the study was enhanced by the use of OFR data to constrain SOA formation potential for up to 3 days of photochemical aging (at 1.5×10^6 molec OH cm^{-3}). The model cases that include multi-generation oxidative aging predict substantial SOA increases after 1.5 days of aging, which is not consistent with the OFR measurements. In contrast, model cases in which aging is omitted and instead SOA yields for VOCs are corrected for gas phase wall-losses in chamber experiments predict little change in the SOA concentration after 1.5 days. These results highlight the uncertainties associated with aging schemes for SOA from VOCs, which are often implemented in SOA models. Implementing instead corrected yields for VOCs results in similar amounts of SOA but formation rates versus time that are more consistent with observations.

Therefore, the model cases with updated VOC yields that account for chamber wall-losses best reproduce the ambient and OFR data. However, while the WOR + ZHAO + MA case appears to represent a slight improvement over the ROB + ZHAO + MA case, as well as over the ROB + ZHAO + TSI and WOR + ZHAO + TSI cases, it is not possible to conclude that one set of parameters is better than the other since the difference in the predictions for these 4 cases (15 % on average) is likely smaller than the uncertainties due to the model setup as well as the lack of a gas-phase fragmentation pathway during aging. Moreover, uncertainties in the vapor wall-loss corrected yields remain, and the correction of the yields has been performed here using data from a limited number of laboratory studies. In particular, the effect of temperature and humidity on gas-wall partitioning needs to be characterized. The results obtained in our work motivate future studies by showing that SOA models using wall-loss corrected yields reproduce observations for a range of photochemical ages at a level of accuracy that it is as good as or better than parameterizations with the uncorrected yields.

In all six of the model cases, a large majority of the urban SOA at Pasadena is the result of P-SVOC and P-IVOC oxidation. While this result alone cannot be taken as conclusive due to the uncertainties in the model parameters, further evidence for the importance of P-SVOCs and P-IVOCs is obtained by analyzing the percentage of SOA formed at long photochemical ages (~1.5 days) as a function of the precursor rate constant. The P-SVOCs and P-IVOCs have rate constants that are similar to highly reactive VOCs that have been previously found to strongly correlate with SOA formation potential measured by the OFR.

1049 Lastly, the modeled volatility distribution of the total (gas and particle phase)
1050 organic mass between $c^* = 10^{-2}$ and 10^{10} $\mu\text{g m}^{-3}$ is analyzed at three ages and compared
1051 against volatility-resolved measurements. While the total concentrations of gas and
1052 particle phase SVOCs are reasonably well simulated, at the same time there are important
1053 differences between the measured and modeled volatility distribution of SVOCs. These
1054 differences highlight the need for further studies of the chemical pathways that may give
1055 rise to SOA in low volatility bins at $c^* = 10^{-2}$ $\mu\text{g m}^{-3}$ and lower.

1057 ACKNOWLEDGEMENTS

1058 This work was partially supported by a Natural Science and Engineering Research
1059 Council of Canada (NSERC) Discovery Grant (RGPIN/05002-2014), le Fonds de
1060 recherche - Nature et technologies (FRQNT) du Québec (2016-PR-192364), and the
1061 Université de Montréal. AMO and JLJ were supported by CARB 11-305 and EPA STAR
1062 83587701-0. This manuscript has not been reviewed by EPA and thus no endorsement
1063 should be inferred. We gratefully acknowledge VOC data provided by J. de Gouw and
1064 J.B. Gilman.

1066 REFERENCES

- 1067 Ahmadov, R. McKeen, S. A. Robinson, A. L. Bahreini, R. Middlebrook, A. M. de Gouw,
1068 J. A. Meagher, J. Hsie, E. Y. Edgerton, E. Shaw, S. and Trainer, M.: A volatility
1069 basis set model for summertime secondary organic aerosols over the eastern
1070 United States in 2006, *J. Geophys. Res.-Atmos.*, 117, D06301, 2012
- 1071 Atkinson, R. and Arey, J.: Atmospheric degradation of volatile organic compounds,
1072 *Chem. Rev.*, 103, 4605-4638, 2003
- 1073 Bahreini, R. Middlebrook, A. M. de Gouw, J. A. Warneke, C. Trainer, M. Brock, C. A.
1074 Stark, H. Brown, S. S. Dube, W. P. Gilman, J. B. Hall, K. Holloway, J. S. Kuster,
1075 W. C. Perring, A. E. Prevot, A. S. H. Schwarz, J. P. Spackman, J. R. Szidat, S.
1076 Wagner, N. L. Weber, R. J. Zotter, P. and Parrish, D. D.: Gasoline emissions
1077 dominate over diesel in formation of secondary organic aerosol mass, *Geophys.*
1078 *Res. Lett.*, 39, L06805, 2012
- 1079 Borbon, A. Gilman, J. B. Kuster, W. C. Grand, N. Chevaillier, S. Colomb, A.
1080 Dolgorouky, C. Gros, V. Lopez, M. Sarda-Estève, R. Holloway, J. Stutz, J.
1081 Petetin, H. McKeen, S. Beekmann, M. Warneke, C. Parrish, D. D. and de Gouw,
1082 J. A.: Emission ratios of anthropogenic volatile organic compounds in northern
1083 mid-latitude megacities: Observations versus emission inventories in Los Angeles
1084 and Paris, *J. Geophys. Res.-Atmos.*, 118, 2041-2057, 2013

1085 Cappa, C. D. and Wilson, K. R.: Multi-generation gas-phase oxidation, equilibrium
 1086 partitioning, and the formation and evolution of secondary organic aerosol,
 1087 *Atmos. Chem. Phys.*, 12, 9505-9528, 2012

1088 Carter, W. P. L.: Development of the SAPRC-07 chemical mechanism, *Atmos. Environ.*,
 1089 44, 5324-5335, 2010

1090 Chan, A. W. H. Kautzman, K. E. Chhabra, P. S. Surratt, J. D. Chan, M. N. Crounse, J. D.
 1091 Kuerten, A. Wennberg, P. O. Flagan, R. C. and Seinfeld, J. H.: Secondary organic
 1092 aerosol formation from photooxidation of naphthalene and alkylnaphthalenes:
 1093 implications for oxidation of intermediate volatility organic compounds (IVOCs),
 1094 *Atmos. Chem. Phys.*, 9, 3049-3060, 2009

1095 Christensen, J. H. Krishna Kumar, K. Aldrian, E. An, S.-I. Cavalcanti, I. F. A. de Castro,
 1096 M. Dong, W. Goswami, A. Hall, A. Kanyanga, J. K. Kitoh, A. Kossin, J. Lau, N.-
 1097 C. Renwick, J. Stephenson, D. B. Xie, S.-P. and Zhou, T.: Climate Change 2013:
 1098 The Physical Scientific Basis. Contribution of Working Group I to the Fifth
 1099 Assessment Report of the Intergovernmental Panel on Climate Change. 2013

1100 De Gouw, J. and Jimenez, J. L.: Organic Aerosols in the Earth's Atmosphere, *Environ.*
 1101 *Sci. Technol.*, 43, 7614-7618, 2009

1102 DeCarlo, P. F. Ulbrich, I. M. Crounse, J. de Foy, B. Dunlea, E. J. Aiken, A. C. Knapp, D.
 1103 Weinheimer, A. J. Campos, T. Wennberg, P. O. and Jimenez, J. L.: Investigation
 1104 of the sources and processing of organic aerosol over the Central Mexican Plateau
 1105 from aircraft measurements during MILAGRO, *Atmos. Chem. Phys.*, 10, 5257-
 1106 5280, 2010

1107 Dockery, D. W. and Pope, C. A.: Acute respiratory effects of particulate air-pollution,
 1108 *Annu. Rev. Publ. Health*, 15, 107-132, 1994

1109 Donahue, N. M. Chuang, W. Epstein, S. A. Kroll, J. H. Worsnop, D. R. Robinson, A. L.
 1110 Adams, P. J. and Pandis, S. N.: Why do organic aerosols exist? Understanding
 1111 aerosol lifetimes using the two-dimensional volatility basis set, *Envir. Chem.*, 10,
 1112 151-157, 2013

1113 Donahue, N. M. Robinson, A. L. Stanier, C. O. and Pandis, S. N.: Coupled partitioning,
 1114 dilution, and chemical aging of semivolatile organics, *Environ. Sci. Technol.*, 40,
 1115 2635-2643, 2006

1116 Dunmore, R. E. Hopkins, J. R. Lidster, R. T. Lee, J. D. Evans, M. J. Rickard, A. R.
 1117 Lewis, A. C. and Hamilton, J. F.: Diesel-related hydrocarbons can dominate gas
 1118 phase reactive carbon in megacities, *Atmos. Chem. Phys.*, 15, 9983-9996, 2015

1119 Dzepina, K. Cappa, C. D. Volkamer, R. M. Madronich, S. DeCarlo, P. F. Zaveri, R. A.
 1120 and Jimenez, J. L.: Modeling the Multiday Evolution and Aging of Secondary
 1121 Organic Aerosol During MILAGRO 2006, *Environ. Sci. Technol.*, 45, 3496-3503,
 1122 2011

- 1123 Dzepina, K. Volkamer, R. M. Madronich, S. Tulet, P. Ulbrich, I. M. Zhang, Q. Cappa, C.
1124 D. Ziemann, P. J. and Jimenez, J. L.: Evaluation of recently-proposed secondary
1125 organic aerosol models for a case study in Mexico City, *Atmos. Chem. Phys.*, 9,
1126 5681-5709, 2009
- 1127 Ervens, B. and Volkamer, R.: Glyoxal processing by aerosol multiphase chemistry:
1128 towards a kinetic modeling framework of secondary organic aerosol formation in
1129 aqueous particles, *Atmos. Chem. Phys.*, 10, 8219-8244, 2010
- 1130 Fountoukis, C. Megaritis, A. G. Skyllakou, K. Charalampidis, P. E. Denier van der Gon,
1131 H. A. C. Crippa, M. Prévôt, A. S. H. Fachinger, F. Wiedensohler, A. Pilinis, C.
1132 and Pandis, S. N.: Simulating the formation of carbonaceous aerosol in a
1133 European Megacity (Paris) during the MEGAPOLI summer and winter
1134 campaigns, *Atmos. Chem. Phys.*, 16, 3727-3741, 2016
- 1135 Gentner, D. R. Isaacman, G. Worton, D. R. Chan, A. W. H. Dallmann, T. R. Davis, L.
1136 Liu, S. Day, D. A. Russell, L. M. Wilson, K. R. Weber, R. J. Guha, A. Harley, R.
1137 A. and Goldstein, A. H.: Elucidating secondary organic aerosol from diesel and
1138 gasoline vehicles through detailed characterization of organic carbon emissions,
1139 *Proc. Natl. Acad. Sci. USA*, 109, 18318-18323, 2012
- 1140 George, I. J. and Abbatt, J. P. D.: Heterogeneous oxidation of atmospheric aerosol
1141 particles by gas-phase radicals, *Nat. Chem.*, 2, 713-722, 2010
- 1142 Grieshop, A. P. Logue, J. M. Donahue, N. M. and Robinson, A. L.: Laboratory
1143 investigation of photochemical oxidation of organic aerosol from wood fires 1:
1144 measurement and simulation of organic aerosol evolution, *Atmos. Chem. Phys.*, 9,
1145 1263-1277, 2009
- 1146 Hallquist, M. Wenger, J. C. Baltensperger, U. Rudich, Y. Simpson, D. Claeys, M.
1147 Dommen, J. Donahue, N. M. George, C. Goldstein, A. H. Hamilton, J. F.
1148 Herrmann, H. Hoffmann, T. Iinuma, Y. Jang, M. Jenkin, M. E. Jimenez, J. L.
1149 Kiendler-Scharr, A. Maenhaut, W. McFiggans, G. Mentel, Th F. Monod, A.
1150 Prevot, A. S. H. Seinfeld, J. H. Surratt, J. D. Szmigielski, R. and Wildt, J.: The
1151 formation, properties and impact of secondary organic aerosol: current and
1152 emerging issues, *Atmos. Chem. Phys.*, 9, 5155-5236, 2009
- 1153 Hayes, P. L. Carlton, A. G. Baker, K. R. Ahmadov, R. Washenfelder, R. A. Alvarez, S.
1154 Rappenglück, B. Gilman, J. B. Kuster, W. C. de Gouw, J. A. Zotter, P. Prévôt, A.
1155 S. H. Szidat, S. Kleindienst, T. E. Offenberg, J. H. Ma, P. K. and Jimenez, J. L.:
1156 Modeling the formation and aging of secondary organic aerosols in Los Angeles
1157 during CalNex 2010, *Atmos. Chem. Phys.*, 15, 5773-5801, 2015
- 1158 Hayes, P. L. Ortega, A. M. Cubison, M. J. Froyd, K. D. Zhao, Y. Cliff, S. S. Hu, W. W.
1159 Toohey, D. W. Flynn, J. H. Lefer, B. L. Grossberg, N. Alvarez, S. Rappenglueck,
1160 B. Taylor, J. W. Allan, J. D. Holloway, J. S. Gilman, J. B. Kuster, W. C. De
1161 Gouw, J. A. Massoli, P. Zhang, X. Liu, J. Weber, R. J. Corrigán, A. L. Russell, L.
1162 M. Isaacman, G. Worton, D. R. Kreisberg, N. M. Goldstein, A. H. Thalman, R.
1163 Waxman, E. M. Volkamer, R. Lin, Y. H. Surratt, J. D. Kleindienst, T. E.

1164 Offenberg, J. H. Dusanter, S. Griffith, S. Stevens, P. S. Brioude, J. Angevine, W.
 1165 M. and Jimenez, J. L.: Organic aerosol composition and sources in Pasadena,
 1166 California, during the 2010 CalNex campaign, *J. Geophys. Res.-Atmos.*, 118,
 1167 9233-9257, 2013

1168 Heald, C. L. Coe, H. Jimenez, J. L. Weber, R. J. Bahreini, R. Middlebrook, A. M.
 1169 Russell, L. M. Jolleys, M. Fu, T. M. Allan, J. D. Bower, K. N. Capes, G. Crosier,
 1170 J. Morgan, W. T. Robinson, N. H. Williams, P. I. Cubison, M. J. DeCarlo, P. F.
 1171 and Dunlea, E. J.: Exploring the vertical profile of atmospheric organic aerosol:
 1172 comparing 17 aircraft field campaigns with a global model, *Atmos. Chem. Phys.*,
 1173 11, 12673-12696, 2011

1174 Hodzic, A. and Jimenez, J. L.: Modeling anthropogenically controlled secondary organic
 1175 aerosols in a megacity: a simplified framework for global and climate models,
 1176 *Geosci. Model Dev.*, 4, 901-917, 2011

1177 Hodzic, A. Jimenez, J. L. Madronich, S. Canagaratna, M. R. DeCarlo, P. F. Kleinman, L.
 1178 and Fast, J.: Modeling organic aerosols in a megacity: potential contribution of
 1179 semi-volatile and intermediate volatility primary organic compounds to secondary
 1180 organic aerosol formation, *Atmos. Chem. Phys.*, 10, 5491-5514, 2010

1181 Hodzic, A. Kasibhatla, P. S. Jo, D. S. Cappa, C. D. Jimenez, J. L. Madronich, S. and
 1182 Park, R. J.: Rethinking the global secondary organic aerosol (SOA) budget:
 1183 stronger production, faster removal, shorter lifetime, *Atmos. Chem. Phys.*, 16,
 1184 7917-7941, 2016

1185 Hu, W. Palm, B. B. Day, D. A. Campuzano-Jost, P. Krechmer, J. E. Peng, Z. de Sá, S. S.
 1186 Martin, S. T. Alexander, M. L. Baumann, K. Hacker, L. Kiendler-Scharr, A.
 1187 Koss, A. R. de Gouw, J. A. Goldstein, A. H. Seco, R. Sjostedt, S. J. Park, J. H.
 1188 Guenther, A. B. Kim, S. Canonaco, F. Prévôt, A. S. H. Brune, W. H. and Jimenez,
 1189 J. L.: Volatility and lifetime against OH heterogeneous reaction of ambient
 1190 isoprene-epoxydiols-derived secondary organic aerosol (IEPOX-SOA), *Atmos.*
 1191 *Chem. Phys.*, 16, 11563-11580, 2016

1192 Jimenez, J. L. Canagaratna, M. R. Donahue, N. M. Prevot, A. S. H. Zhang, Q. Kroll, J. H.
 1193 DeCarlo, P. F. Allan, J. D. Coe, H. Ng, N. L. Aiken, A. C. Docherty, K. S.
 1194 Ulbrich, I. M. Grieshop, A. P. Robinson, A. L. Duplissy, J. Smith, J. D. Wilson,
 1195 K. R. Lanz, V. A. Hueglin, C. Sun, Y. L. Tian, J. Laaksonen, A. Raatikainen, T.
 1196 Rautiainen, J. Vaattovaara, P. Ehn, M. Kulmala, M. Tomlinson, J. M. Collins, D.
 1197 R. Cubison, M. J. Dunlea, E. J. Huffman, J. A. Onasch, T. B. Alfarra, M. R.
 1198 Williams, P. I. Bower, K. Kondo, Y. Schneider, J. Drewnick, F. Borrmann, S.
 1199 Weimer, S. Demerjian, K. Salcedo, D. Cottrell, L. Griffin, R. Takami, A.
 1200 Miyoshi, T. Hatakeyama, S. Shimono, A. Sun, J. Y. Zhang, Y. M. Dzepina, K.
 1201 Kimmel, J. R. Sueper, D. Jayne, J. T. Herndon, S. C. Trimborn, A. M. Williams,
 1202 L. R. Wood, E. C. Middlebrook, A. M. Kolb, C. E. Baltensperger, U. and
 1203 Worsnop, D. R.: Evolution of Organic Aerosols in the Atmosphere, *Science*, 326,
 1204 1525-1529, 2009

- 1205 Klein, F. Platt, S. M. Farren, N. J. Detournay, A. Bruns, E. A. Bozzetti, C. Daellenbach,
1206 K. R. Kilic, D. Kumar, N. K. Pieber, S. M. Slowik, J. G. Temime-Roussel, B.
1207 Marchand, N. Hamilton, J. F. Baltensperger, U. Prevot, A. S. H. and El Haddad,
1208 I.: Characterization of Gas-Phase Organics Using Proton Transfer Reaction Time-
1209 of-Flight Mass Spectrometry: Cooking Emissions, *Environ. Sci. Technol.*, 50,
1210 1243-1250, 2016
- 1211 Knote, C. Hodzic, A. Jimenez, J. L. Volkamer, R. Orlando, J. J. Baidar, S. Brioude, J.
1212 Fast, J. Gentner, D. R. Goldstein, A. H. Hayes, P. L. Knighton, W. B. Oetjen, H.
1213 Setyan, A. Stark, H. Thalman, R. Tyndall, G. Washenfelder, R. Waxman, E. and
1214 Zhang, Q.: Simulation of semi-explicit mechanisms of SOA formation from
1215 glyoxal in aerosol in a 3-D model, *Atmos. Chem. Phys.*, 14, 6213-6239, 2014
- 1216 Krechmer, J. E. Pagonis, D. Ziemann, P. J. and Jimenez, J. L.: Quantification of Gas-
1217 Wall Partitioning in Teflon Environmental Chambers Using Rapid Bursts of Low-
1218 Volatility Oxidized Species Generated in Situ, *Environ. Sci. Technol.*, 50, 5757-
1219 5765, 2016
- 1220 Kroll, J. H. Ng, N. L. Murphy, S. M. Flagan, R. C. and Seinfeld, J. H.: Secondary organic
1221 aerosol formation from isoprene photooxidation, *Environ. Sci. Technol.*, 40,
1222 1869-1877, 2006
- 1223 Liu, T. Li, Z. Chan, M. and Chan, C. K.: Formation of secondary organic aerosols from
1224 gas-phase emissions of heated cooking oils, *Atmos. Chem. Phys. Discuss.*, 2017,
1225 1-30, 2017
- 1226 Matsunaga, A. and Ziemann, P. J.: Gas-Wall Partitioning of Organic Compounds in a
1227 Teflon Film Chamber and Potential Effects on Reaction Product and Aerosol
1228 Yield Measurements, *Aerosol Sci. Technol.*, 44, 881-892, 2010
- 1229 McDonald, B. C. Goldstein, A. H. and Harley, R. A.: Long-Term Trends in California
1230 Mobile Source Emissions and Ambient Concentrations of Black Carbon and
1231 Organic Aerosol, *Environ. Sci. Technol.*, 49, 5178-5188, 2015
- 1232 Ng, N. L. Kroll, J. H. Chan, A. W. H. Chhabra, P. S. Flagan, R. C. and Seinfeld, J. H.:
1233 Secondary organic aerosol formation from m-xylene, toluene, and benzene,
1234 *Atmos. Chem. Phys.*, 7, 3909-3922, 2007
- 1235 Odum, J. R. Hoffmann, T. Bowman, F. Collins, D. Flagan, R. C. and Seinfeld, J. H.:
1236 Gas/particle partitioning and secondary organic aerosol yields, *Environ. Sci.*
1237 *Technol.*, 30, 2580-2585, 1996
- 1238 Ortega, A. M. Hayes, P. L. Peng, Z. Palm, B. B. Hu, W. Day, D. A. Li, R. Cubison, M. J.
1239 Brune, W. H. Graus, M. Warneke, C. Gilman, J. B. Kuster, W. C. de Gouw, J.
1240 Gutiérrez-Montes, C. and Jimenez, J. L.: Real-time measurements of secondary
1241 organic aerosol formation and aging from ambient air in an oxidation flow reactor
1242 in the Los Angeles area, *Atmos. Chem. Phys.*, 16, 7411-7433, 2016

- 1243 Ots, R. Young, D. E. Vieno, M. Xu, L. Dunmore, R. E. Allan, J. D. Coe, H. Williams, L.
 1244 R. Herndon, S. C. Ng, N. L. Hamilton, J. F. Bergström, R. Di Marco, C. Nemitz,
 1245 E. Mackenzie, I. A. Kuenen, J. J. P. Green, D. C. Reis, S. and Heal, M. R.:
 1246 Simulating secondary organic aerosol from missing diesel-related intermediate-
 1247 volatility organic compound emissions during the Clean Air for
 1248 London (ClearfLo) campaign, *Atmos. Chem. Phys.*, 16, 6453-6473, 2016
- 1249 Palm, B. B. Campuzano-Jost, P. Ortega, A. M. Day, D. A. Kaser, L. Jud, W. Karl, T.
 1250 Hansel, A. Hunter, J. F. Cross, E. S. Kroll, J. H. Peng, Z. Brune, W. H. and
 1251 Jimenez, J. L.: In situ secondary organic aerosol formation from ambient pine
 1252 forest air using an oxidation flow reactor, *Atmos. Chem. Phys.*, 16, 2943-2970,
 1253 2016
- 1254 Pankow, J. F.: An absorption model of the gas aerosol partitioning involved in the
 1255 formation of secondary organic aerosol, *Atmos. Environ.*, 28, 189-193, 1994
- 1256 Pankow, J. F. and Asher, W. E.: SIMPOL.1: a simple group contribution method for
 1257 predicting vapor pressures and enthalpies of vaporization of multifunctional
 1258 organic compounds, *Atmos. Chem. Phys.*, 8, 2773-2796, 2008
- 1259 Parrish, D. D. Stohl, A. Forster, C. Atlas, E. L. Blake, D. R. Goldan, P. D. Kuster, W. C.
 1260 and de Gouw, J. A.: Effects of mixing on evolution of hydrocarbon ratios in the
 1261 troposphere, *J. Geophys. Res.-Atmos.*, 112, 2007
- 1262 Presto, A. A. Miracolo, M. A. Donahue, N. M. and Robinson, A. L.: Secondary Organic
 1263 Aerosol Formation from High-NO_x Photo-Oxidation of Low Volatility
 1264 Precursors: n-Alkanes, *Environ. Sci. Technol.*, 44, 2029-2034, 2010
- 1265 Robinson, A. L. Donahue, N. M. Shrivastava, M. K. Weitkamp, E. A. Sage, A. M.
 1266 Grieshop, A. P. Lane, T. E. Pierce, J. R. and Pandis, S. N.: Rethinking organic
 1267 aerosols: Semivolatile emissions and photochemical aging, *Science*, 315, 1259-
 1268 1262, 2007
- 1269 Ryerson, T. B. Andrews, A. E. Angevine, W. M. Bates, T. S. Brock, C. A. Cairns, B.
 1270 Cohen, R. C. Cooper, O. R. de Gouw, J. A. Fehsenfeld, F. C. Ferrare, R. A.
 1271 Fischer, M. L. Flagan, R. C. Goldstein, A. H. Hair, J. W. Hardesty, R. M.
 1272 Hostetler, C. A. Jimenez, J. L. Langford, A. O. McCauley, E. McKeen, S. A.
 1273 Molina, L. T. Nenes, A. Oltmans, S. J. Parrish, D. D. Pederson, J. R. Pierce, R. B.
 1274 Prather, K. Quinn, P. K. Seinfeld, J. H. Senff, C. J. Sorooshian, A. Stutz, J.
 1275 Surratt, J. D. Trainer, M. Volkamer, R. Williams, E. J. and Wofsy, S. C.: The
 1276 2010 California Research at the Nexus of Air Quality and Climate Change
 1277 (CalNex) field study, *J. Geophys. Res.-Atmos.*, 118, 5830-5866, 2013
- 1278 Shrivastava, M. Easter, R. C. Liu, X. H. Zelenyuk, A. Singh, B. Zhang, K. Ma, P. L.
 1279 Chand, D. Ghan, S. Jimenez, J. L. Zhang, Q. Fast, J. Rasch, P. J. and Tiitta, P.:
 1280 Global transformation and fate of SOA: Implications of low-volatility SOA and
 1281 gas-phase fragmentation reactions, *J. Geophys. Res.-Atmos.*, 120, 4169-4195,
 1282 2015

1283 Shrivastava, M. Fast, J. Easter, R. Gustafson Jr, W. I. Zaveri, R. A. Jimenez, J. L. Saide,
 1284 P. and Hodzic, A.: Modeling organic aerosols in a megacity: comparison of
 1285 simple and complex representations of the volatility basis set approach, *Atmos.*
 1286 *Chem. Phys.*, 11, 6639-6662, 2011

1287 Shrivastava, M. Zelenyuk, A. Imre, D. Easter, R. Beranek, J. Zaveri, R. A. and Fast, J.:
 1288 Implications of low volatility SOA and gas-phase fragmentation reactions on
 1289 SOA loadings and their spatial and temporal evolution in the atmosphere, *J.*
 1290 *Geophys. Res.-Atmos.*, 118, 3328-3342, 2013

1291 Spracklen, D. V. Jimenez, J. L. Carslaw, K. S. Worsnop, D. R. Evans, M. J. Mann, G. W.
 1292 Zhang, Q. Canagaratna, M. R. Allan, J. Coe, H. McFiggans, G. Rap, A. and
 1293 Forster, P.: Aerosol mass spectrometer constraint on the global secondary organic
 1294 aerosol budget, *Atmos. Chem. Phys.*, 11, 12109-12136, 2011

1295 Tsimpidi, A. P. Karydis, V. A. Zavala, M. Lei, W. Molina, L. Ulbrich, I. M. Jimenez, J.
 1296 L. and Pandis, S. N.: Evaluation of the volatility basis-set approach for the
 1297 simulation of organic aerosol formation in the Mexico City metropolitan area,
 1298 *Atmos. Chem. Phys.*, 10, 525-546, 2010

1299 Volkamer, R. Jimenez, J. L. San Martini, F. Dzepina, K. Zhang, Q. Salcedo, D. Molina,
 1300 L. T. Worsnop, D. R. and Molina, M. J.: Secondary organic aerosol formation
 1301 from anthropogenic air pollution: Rapid and higher than expected, *Geophys. Res.*
 1302 *Lett.*, 33, 2006

1303 Warneke, C. de Gouw, J. A. Holloway, J. S. Peischl, J. Ryerson, T. B. Atlas, E. Blake, D.
 1304 Trainer, M. and Parrish, D. D.: Multiyear trends in volatile organic compounds in
 1305 Los Angeles, California: Five decades of decreasing emissions, *J. Geophys. Res.-*
 1306 *Atmos.*, 117, 2012

1307 Warneke, C. McKeen, S. A. de Gouw, J. A. Goldan, P. D. Kuster, W. C. Holloway, J. S.
 1308 Williams, E. J. Lerner, B. M. Parrish, D. D. Trainer, M. Fehsenfeld, F. C. Kato, S.
 1309 Atlas, E. L. Baker, A. and Blake, D. R.: Determination of urban volatile organic
 1310 compound emission ratios and comparison with an emissions database, *J.*
 1311 *Geophys. Res.-Atmos.*, 112, D10s47, 2007

1312 Washenfelder, R. A. Young, C. J. Brown, S. S. Angevine, W. M. Atlas, E. L. Blake, D.
 1313 R. Bon, D. M. Cubison, M. J. de Gouw, J. A. Dusanter, S. Flynn, J. Gilman, J. B.
 1314 Graus, M. Griffith, S. Grossberg, N. Hayes, P. L. Jimenez, J. L. Kuster, W. C.
 1315 Lefer, B. L. Pollack, I. B. Ryerson, T. B. Stark, H. Stevens, P. S. and Trainer, M.
 1316 K.: The glyoxal budget and its contribution to organic aerosol for Los Angeles,
 1317 California, during CalNex 2010, *J. Geophys. Res.-Atmos.*, 116, 2011

1318 Watson, J. G.: Visibility: Science and regulation, *J. Air Waste Manag. Assoc.*, 52, 628-
 1319 713, 2002

1320 Woody, M. C. Baker, K. R. Hayes, P. L. Jimenez, J. L. Koo, B. and Pye, H. O. T.:
 1321 Understanding sources of organic aerosol during CalNex-2010 using the CMAQ-
 1322 VBS, *Atmos. Chem. Phys.*, 16, 4081-4100, 2016

- 1323 Worton, D. R. Isaacman, G. Gentner, D. R. Dallmann, T. R. Chan, A. W. H. Ruehl, C.
 1324 Kirchstetter, T. W. Wilson, K. R. Harley, R. A. and Goldstein, A. H.: Lubricating
 1325 Oil Dominates Primary Organic Aerosol Emissions from Motor Vehicles,
 1326 Environ. Sci. Technol., 48, 3698-3706, 2014
- 1327 Ye, P. Ding, X. Hakala, J. Hofbauer, V. Robinson, E. S. and Donahue, N. M.: Vapor wall
 1328 loss of semi-volatile organic compounds in a Teflon chamber, Aerosol Sci.
 1329 Technol., 50, 822-834, 2016
- 1330 Yuan, B. Veres, P. R. Warneke, C. Roberts, J. M. Gilman, J. B. Koss, A. Edwards, P. M.
 1331 Graus, M. Kuster, W. C. Li, S. M. Wild, R. J. Brown, S. S. Dubé, W. P. Lerner,
 1332 B. M. Williams, E. J. Johnson, J. E. Quinn, P. K. Bates, T. S. Lefer, B. Hayes, P.
 1333 L. Jimenez, J. L. Weber, R. J. Zamora, R. Ervens, B. Millet, D. B. Rappenglück,
 1334 B. and de Gouw, J. A.: Investigation of secondary formation of formic acid: urban
 1335 environment vs. oil and gas producing region, Atmos. Chem. Phys., 15, 1975-
 1336 1993, 2015
- 1337 Zhang, Q. Jimenez, J. L. Canagaratna, M. R. Allan, J. D. Coe, H. Ulbrich, I. Alfarra, M.
 1338 R. Takami, A. Middlebrook, A. M. Sun, Y. L. Dzepina, K. Dunlea, E. Docherty,
 1339 K. DeCarlo, P. F. Salcedo, D. Onasch, T. Jayne, J. T. Miyoshi, T. Shimono, A.
 1340 Hatakeyama, S. Takegawa, N. Kondo, Y. Schneider, J. Drewnick, F. Borrmann,
 1341 S. Weimer, S. Demerjian, K. Williams, P. Bower, K. Bahreini, R. Cottrell, L.
 1342 Griffin, R. J. Rautiainen, J. Sun, J. Y. Zhang, Y. M. and Worsnop, D. R.: Ubiquity
 1343 and dominance of oxygenated species in organic aerosols in anthropogenically-
 1344 influenced Northern Hemisphere midlatitudes, Geophys. Res. Lett., 34, 2007
- 1345 Zhang, X. Cappa, C. D. Jathar, S. H. McVay, R. C. Ensberg, J. J. Kleeman, M. I. J. and
 1346 Seinfeld, J. H.: Influence of vapor wall loss in laboratory chambers on yields of
 1347 secondary organic aerosol, Proc. Natl. Acad. Sci. USA, 111, 5802-5807, 2014
- 1348 Zhao, Y. Hennigan, C. J. May, A. A. Tkacik, D. S. de Gouw, J. A. Gilman, J. B. Kuster,
 1349 W. C. Borbon, A. and Robinson, A. L.: Intermediate-Volatility Organic
 1350 Compounds: A Large Source of Secondary Organic Aerosol, Environ. Sci.
 1351 Technol., 48, 13743-13750, 2014
- 1352 Zotter, P. El-Haddad, I. Zhang, Y. M. Hayes, P. L. Zhang, X. Lin, Y.-H. Wacker, L.
 1353 Schnelle-Kreis, J. Abbaszade, G. Zimmermann, R. Surratt, J. D. Weber, R. J.
 1354 Jimenez, J. L. Szidat, S. Baltensperger, U. and Prevot, A. S. H.: Diurnal cycle of
 1355 fossil and nonfossil carbon using radiocarbon analyses during CalNex, J.
 1356 Geophys. Res.-Atmos., 119, 6818-6835, 2014

1357

1358 **Table 1.** Summary of the model cases used in this paper.

Case	Notes	References
1) ROB + TSI	<u>P-S/IVOCs</u> : Robinson et al. parameterization, and all SOA treated within VBS framework <u>VOCs</u> : Tsimpidi et al. parameterization with aging	Hayes et al. (2015) Robinson et al. (2007) Tsimpidi et al. (2010)
2) ROB + ZHAO + TSI	<u>P-SVOCs</u> : Robinson et al. parameterization, and all SOA treated within VBS framework <u>P-IVOCs</u> : Zhao et al. parameterization with aging <u>VOCs</u> : Tsimpidi et al. parameterization with aging	Robinson et al. (2007) Zhao et al. (2014) Tsimpidi et al. (2010)
3) WOR + ZHAO + TSI	<u>P-SVOCs</u> : Worton et al. volatility distribution for vehicular P-SVOCs, Robinson et al. volatility distribution for cooking P-SVOCs <u>P-IVOCs</u> : Zhao et al. parameterization with aging <u>VOCs</u> : Tsimpidi et al. parameterization with aging	Robinson et al. (2007) Worton et al. (2014) Zhao et al. (2014) Tsimpidi et al. (2010)
4) ROB + MA	<u>P-S/IVOCs</u> : Robinson et al. parameterization, and all SOA treated within VBS framework <u>VOCs</u> : VOCs yields corrected for wall-losses, no aging of VOC oxidation products	Robinson et al. (2007) This work
5) ROB + ZHAO + MA	<u>P-SVOCs</u> : Robinson et al. parameterization, and all SOA treated within VBS framework <u>P-IVOCs</u> : Zhao et al. IVOC parameterization with aging <u>VOCs</u> : VOCs yields corrected for wall-losses, no aging of VOC oxidation products	Robinson et al. (2007) Zhao et al. (2014) This work
6) WOR + ZHAO + MA	<u>P-SVOCs</u> : Worton et al. volatility distribution for vehicular P-SVOCs, Robinson et al. volatility distribution for cooking P-SVOCs <u>P-IVOCs</u> : Zhao et al. IVOC parameterization with aging <u>VOCs</u> : VOCs yields corrected for wall-losses, no aging of VOC oxidation products	Robinson et al. (2007) Worton et al. (2014) Zhao et al. (2014) This work

1359

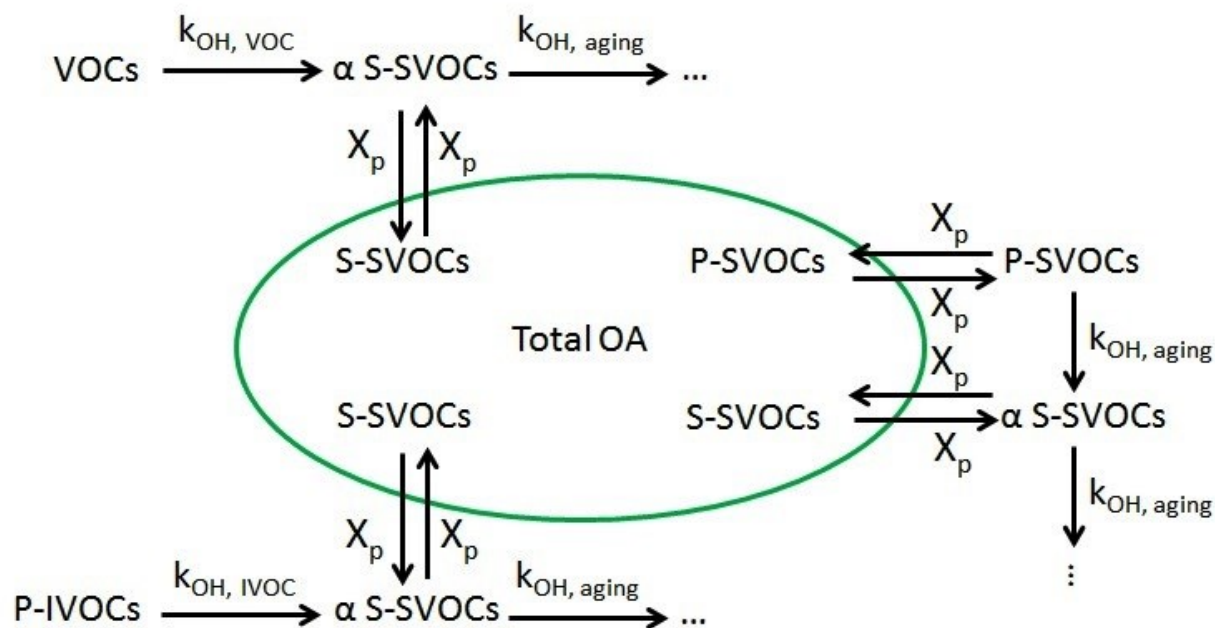


Figure 1. Schematic of the chemical pathways leading to the formation of SOA in the box model where α is the SOA yield, $k_{\text{OH, VOC}}$ and $k_{\text{OH, IVOC}}$ are the rate constants of a VOC or an IVOC species respectively for oxidation by OH radicals, and X_p is the particle-phase fraction of a species.

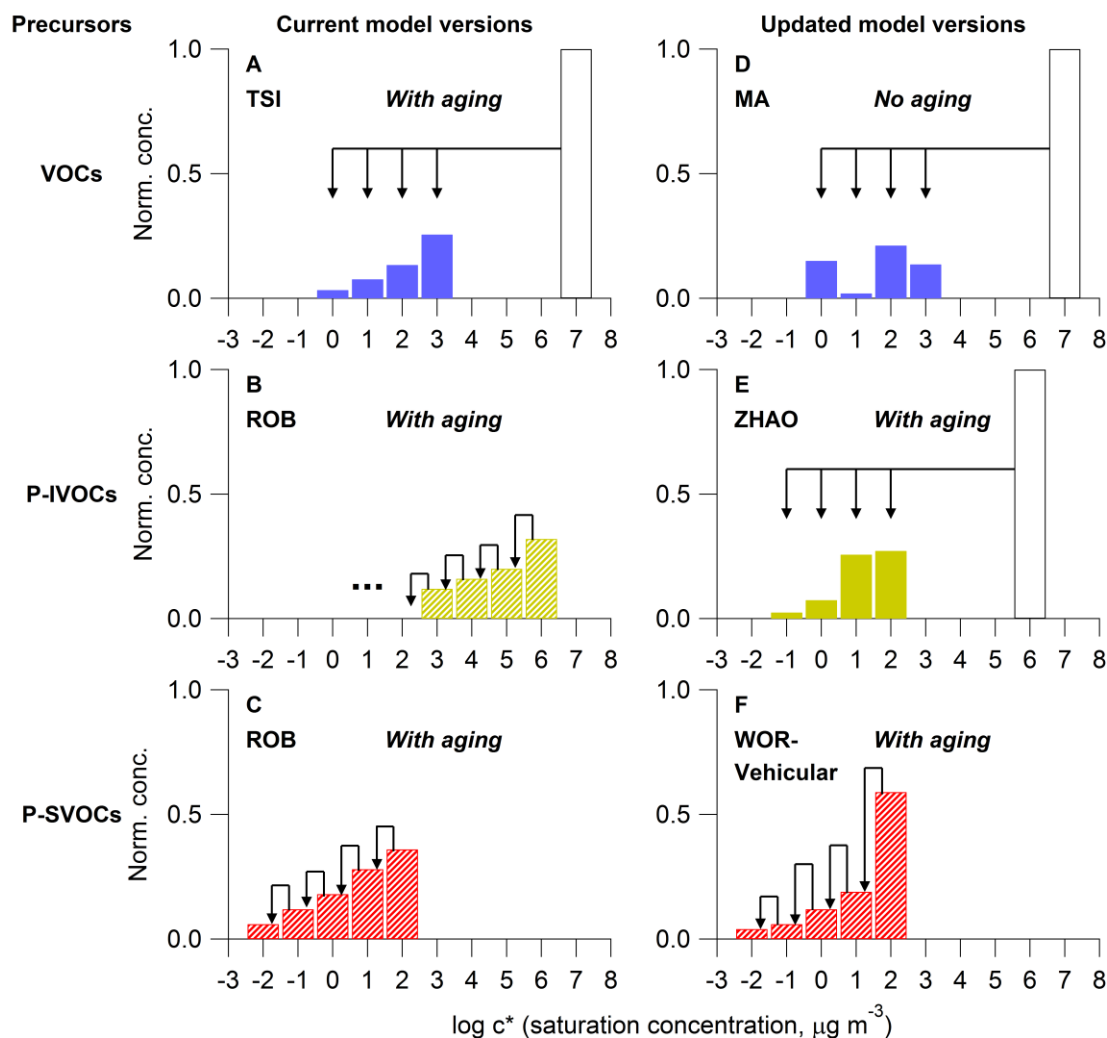


Figure 2. Schematic of the SOA formation parameterizations used in the model. The products formed are shown in different colors for each precursor. Note that the striped color bars indicate that the bins contain both primary and secondary organics. In panel (A) the parameterization of Tsimpidi et al. (2010) distributes the products of VOCs oxidation into four volatility bins. Panels (B) and (C), show the parameterization of Robinson et al. (2007) in which the volatility of the SOA precursors, specifically IVOCs and SVOCs, decrease by one order of magnitude per oxidation reaction. For P-IVOCs, aging continues to transfer mass to lower volatility bins ($\log c^* < 2$). Panel (D) shows the updated parameterization for VOC oxidation that accounts for gas phase wall losses, and Panel (E) shows the updated parameterization for P-IVOC oxidation that uses the speciated measurements of IVOCs from Zhao et al. (2014). In Panel (F), for the parameterization based on the measurements of Worton et al. (2014), the Robinson et al. (2007) volatility distribution is still used for the P-SVOCs emitted from cooking sources. Arrows representing the aging of SOA are omitted for clarity.

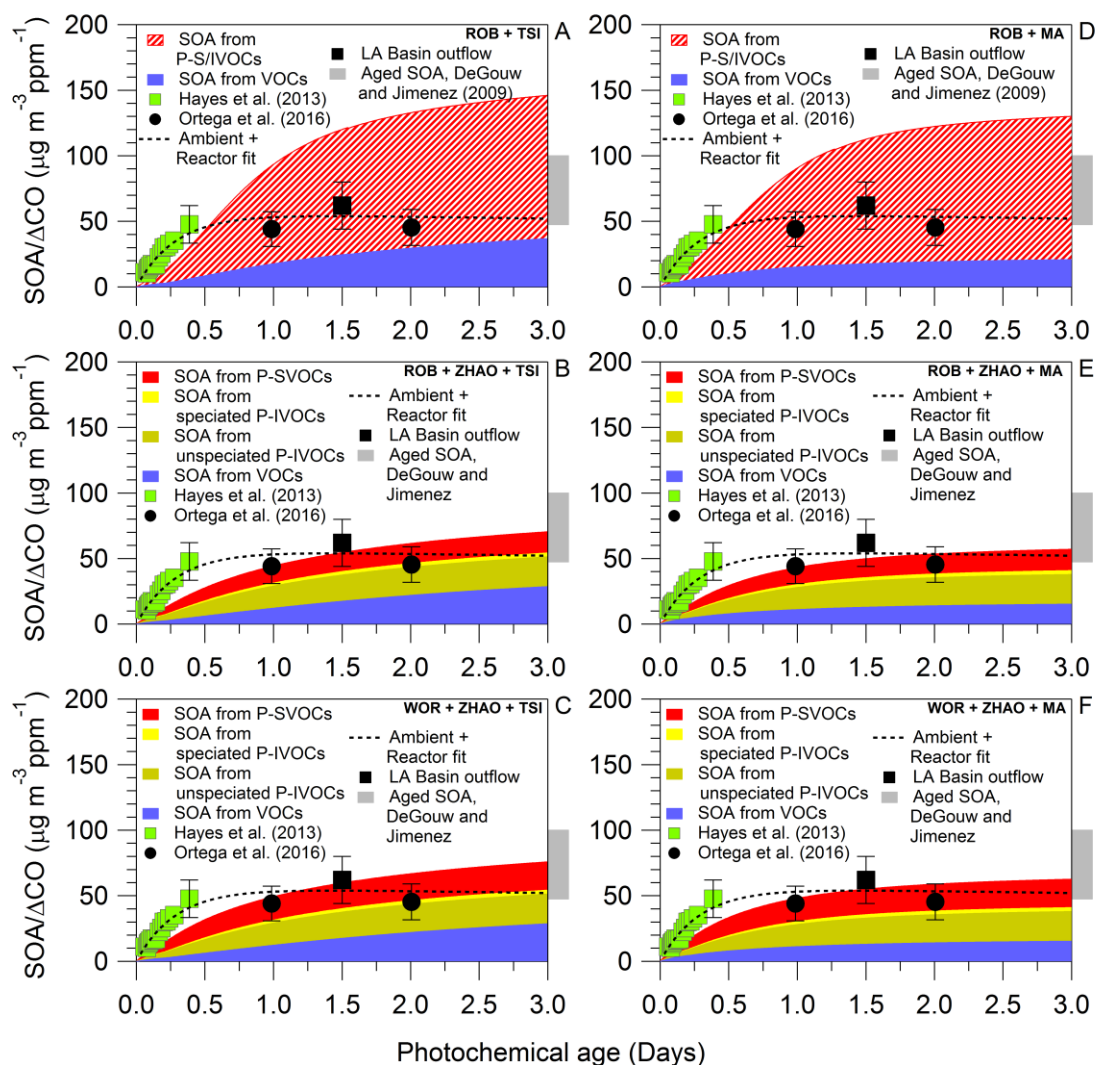


Figure 3. Predicted urban SOA mass by all six cases for up to 3 days of photochemical aging using a reference OH radical concentration of 1.5×10^6 molec cm^{-3} . Background SOA is not included in the figure. The SOA concentrations have been normalized to the background subtracted CO (ΔCO) concentration to account for changes in emission strengths and dilution. The SOA/ ΔCO data determined from the ambient and OFR measurements at Pasadena as reported by Hayes et al. (2013) (green squares) and Ortega et al. (2016) (black circles) are shown. Also shown is SOA/ ΔCO determined from measurements performed aboard the NOAA P3 research aircraft (black square) reported by Bahreini et al. (2012) and highly aged urban air masses (gray bar) reported by de Gouw and Jimenez (2009). The fit for ambient and reactor data reported by Ortega et al. (2016) is also shown (dotted black line).

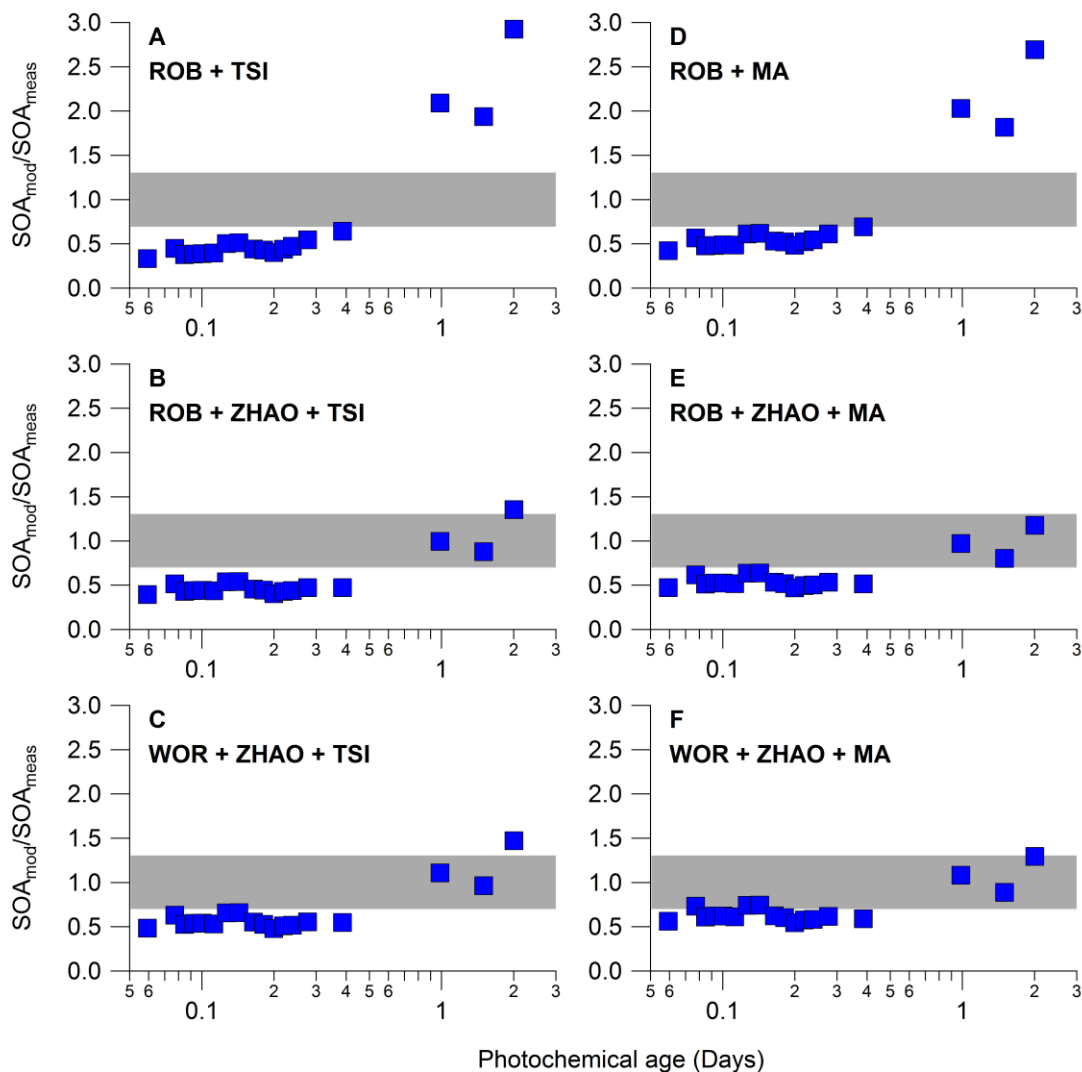


Figure 4. The ratio of the modeled-to-measured SOA concentrations (blue squares) for all model cases. The measurements are the same as used in Figure 3. The gray bar indicates ratios that would correspond to model results that are within the estimated $\pm 30\%$ uncertainty of the measurements.

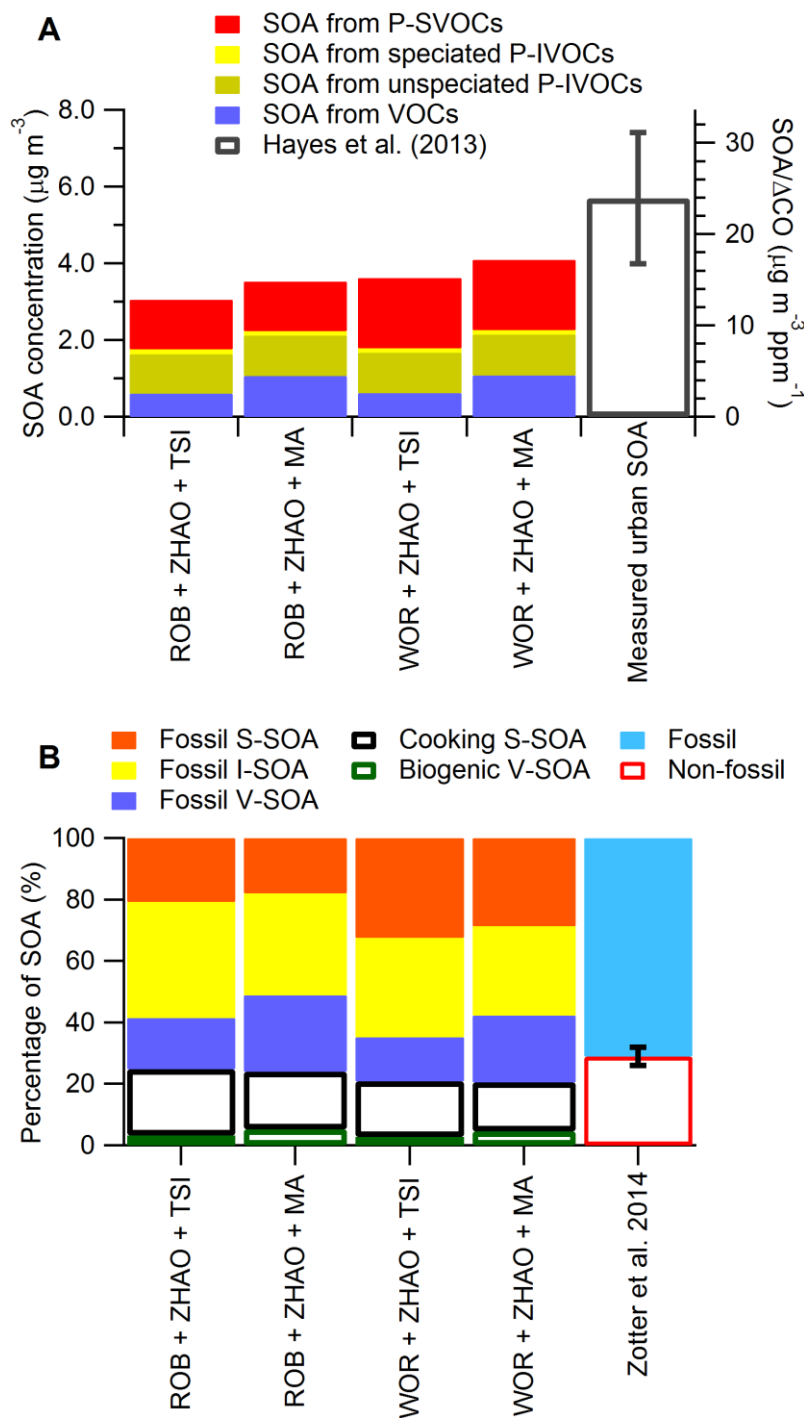


Figure 5. (A) Predicted and measured urban SOA mass for 12:00 – 15:00 local time at the Pasadena ground site. **(B)** The fractional mass of fossil S-SOA, fossil I-SOA, and fossil V-SOA, as well as cooking S-SOA and biogenic V-SOA for the same time and location. The percentage of urban SOA from fossil and non-fossil sources as reported in Zotter et al. (2014) is also displayed. The fossil sources are shown as solid bars and the non-fossil sources as hollow bars.

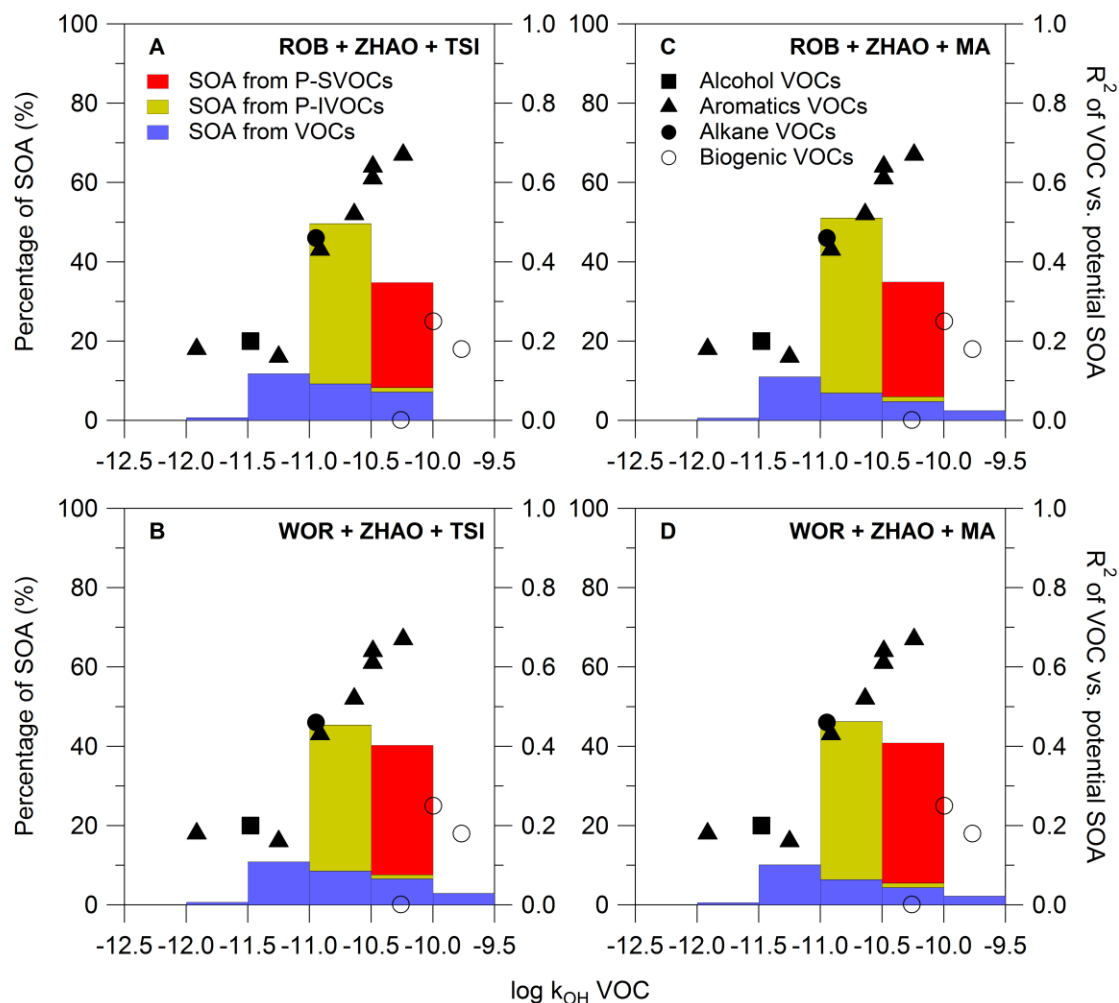
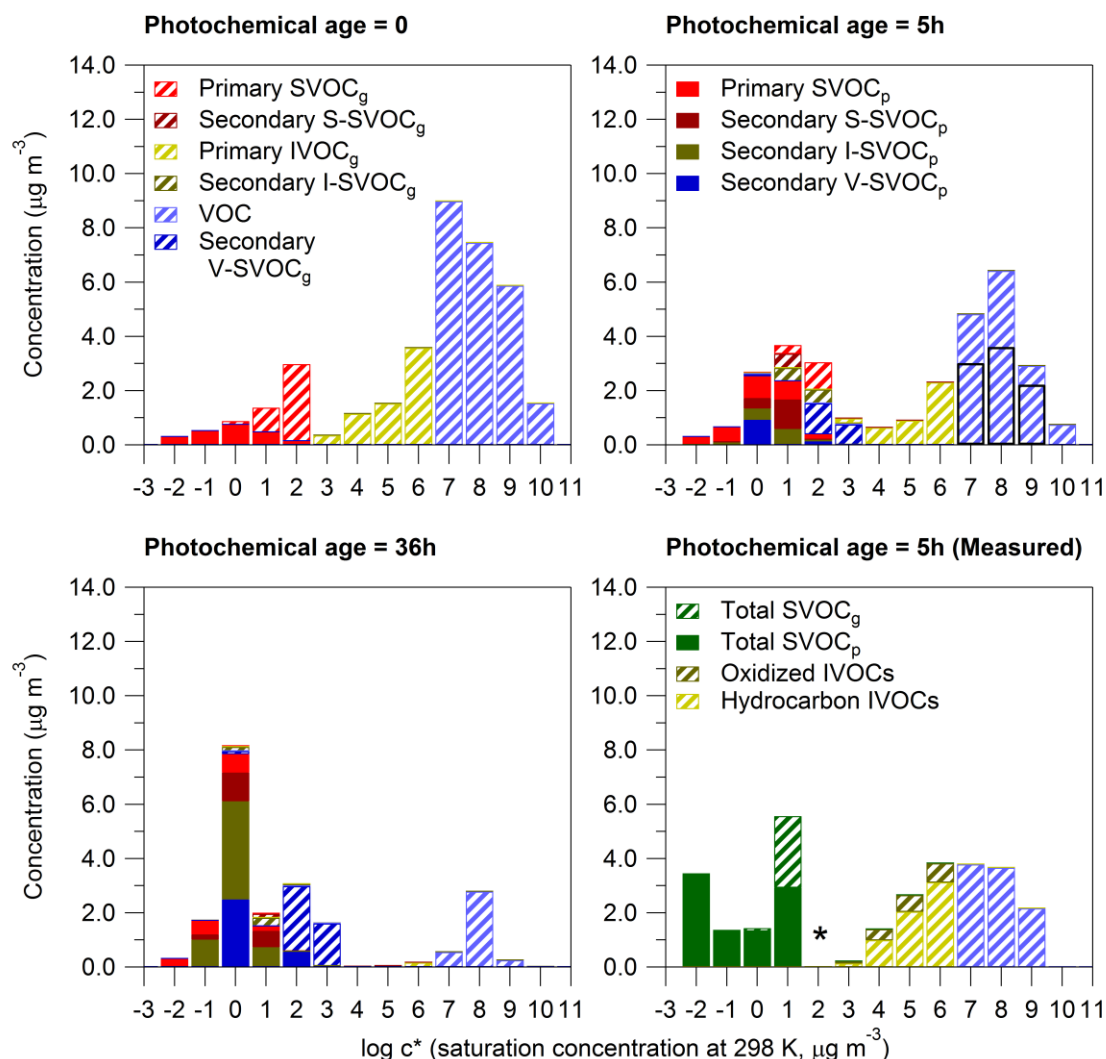


Figure 6. Percentage of SOA mass formed from different precursors at 1.5 days of photochemical aging (at $1.5 \times 10^6 \text{ molec OH cm}^{-3}$) binned according to precursor rate constant. The correlations (R^2) between the concentrations of different VOCs and the maximum SOA concentration formed in the OFR as reported by Ortega et al. (2016) are represented by the markers. The shape of the marker indicates the chemical family to which each compound belongs. For the VOCs and the P-IVOCs the rate constant is the constant for the initial oxidation reaction. The measurements of IVOCs used here allow the rate constants of these precursors to be taken from published work or estimated using structure-activity relationships as described previously (Zhao et al., 2014). For S-SOA, the rate constant is the aging rate constant reported originally by Robinson et al. (2007).



1413

1414 **Figure 7.** OA volatility distribution as simulated by the WOR + ZHAO + MA case displayed at
 1415 different photochemical ages (0, 5, and 36 h). The partitioning of the species is indicated using
 1416 patterned bars for gas phase and solid bars for particle phase mass. The bottom-right graph also
 1417 shows the measured volatility distribution of OA. The SVOC volatility distribution is determined
 1418 using a combined thermal denuder AMS system as described in the supporting information. The
 1419 IVOC volatility distribution was previously published in Zhao et al. (2014), and the VOC
 1420 distribution was determined from GC-MS measurements using the SIMPOL.1 model to estimate
 1421 the volatility of each VOC. The asterisk in the bin $\log c^* = 2$ indicates that measurements are not
 1422 available for this bin. It should be noted that not all the VOCs in the model were measured at
 1423 Pasadena (see text for details). For direct visual comparison with the measurements, the
 1424 simulated concentrations of only the VOCs measured at Pasadena are indicated by the black
 1425 hollow bars in the bins $\log c^* = 7, 8$, and $9 \mu\text{g m}^{-3}$.